Publication Year	2019
Acceptance in OA	2021-01-04T10:37:45Z
Title	Nature, distribution and origin of CO2 on Enceladus
Authors	Combe, Jean-Philippe, McCord, Thomas B., Matson, Dennis L., Johnson, Torrence V., Davies, Ashley G., Scipioni, Francesca, TOSI, Federico
Publisher's version (DOI)	10.1016/j.icarus.2018.08.007
Handle	http://hdl.handle.net/20.500.12386/29415
Journal	ICARUS
Volume	317

Nature, distribution and origin of CO_2 on Enceladus

Jean-Philippe Combe[1], Thomas B. McCord[1], Dennis Matson[1], Torrence Johnson[2], Ashley Gerard Davies[2], Francesca Scipioni[3], Federico Tosi[4],

[1]Bear Fight Institute, 22 Fiddler's Road, P.O. Box 667, Winthrop, WA 98862, USA (jean-philippe_combe @ bearfightinstitute.com / Fax: +001-509-996-3772).

[2]Jet Propulsion Laboratory-California Institute of Technology, Pasadena, CA, USA

[3] NASA Ames Research Center - Moffetr Boulevard, Mountain View, CA, USA

[4]IAPS – INAF, Rome, Italy

Contents

Abstract

We present the first map of CO_2 at the surface of Enceladus using data obtained by the *Cassini* Visible-Infrared Mapping Spectrometer (VIMS). In order to measure the weak and narrow CO_2 absorption band depths around 4.26 µm, we improved: (1) the calibration of VIMS spectra; (2) the calculation of geographic coordinates; and (3) the projection techniques. We averaged multiple observations of a given area to obtain a signal to noise ratio high enough to map the CO_2 abundances. CO_2 is reliably detected mostly in the South Polar Region. This region includes active faults (Tiger Stripes), the highest observed surface temperatures, and locations of active plume eruptions. The occurrence here of CO_2 is consistent with an endogenic origin controlled by tectonics. Both pure CO_2 ice and complexed CO_2 are detected from the positions of absorption bands between 4.27 and 4.24 µm. The highest concentrations of CO_2 are between the main active faults of the South Polar Region, where the surface temperature is low. Pure CO_2 ice deposits at the surface of Enceladus are best modeled by the formation of gas pockets below the icy crust and above the surface of the internal ocean. These pockets eventually release cold CO_2 gas (~70 - ~119 K) at low-velocity (seeping) between the Tiger Stripes [Matson et al., 2018, Icarus, 302, 18-26]. CO_2 clathrate hydrates may form in the ocean and may be subsequently released when a CO_2 gas pocket blows out and erupts. Other mechanisms may contribute to reinforcing the anti-correlation of the CO_2 distribution (of any type) with respect to the location of the Tiger Stripes, such as successive sublimation of CO_2 and condensation on colder areas, and partial frost cover by H_2O releases from plume eruptions.

Highlights

- We present the first map of CO_2 at the surface of Enceladus by *Cassini* VIMS.
- The distribution of CO_2 in the South Polar Region suggests an endogenic origin and control by tectonic activity.
- High surface temperature likely explains why the highest concentrations of CO_2 are measured between the Tiger Stripes and not directly on them.
- Pure surface CO_2 could be vented at low-velocity (seeping) as a cold gas (~70 - ~119 K) from gas pockets that form between the internal ocean and the ice lid along the main active faults.
- Complexed CO_2 is detected.
- CO_2 clathrate hydrates, which form crystal structures, may originate in the internal ocean and may be eventually released to the surface by gas pocket eruptions.

1. Introduction

Plumes of material are observed erupting from four linear depressions in the South Polar Region (SPR) of the Saturnian satellite Enceladus (Dougherty et al., 2006; Hansen et al., 2006; Porco et al., 2006), which is evidence for geophysical processes operating today within Enceladus (Fig. 1). These depressions have distinctive albedo (darker) and color (bluer) than most of Enceladus' surface and are known by the colloquial name of Tiger Stripes (Porco et al., 2006; Johnson, 2005). The Tiger Stripes consist of four subparallel active faults ~130 km long, ~2 km wide, separated by ~35 km on average. Each fault is about 500 m deep and bordered by a 100 m high ridge (Porco et al., 2006). Since the beginning of the *Cassini* mission, the Ion Neutral Mass Spectrometer (INMS, Waite et al., 2004) and the Visual and Infrared Imaging Spectrometer (VIMS, Brown et al., 2004) have been used to determine the composition of the erupting material. Both INMS (Waite et al., 2006, 2009; Glain et al., 2015; Bouquet et al., 2015) and VIMS (Hansen et al., 2006, 2011) indicate that water vapor is the main component. The current quantitative compositional estimates (Waite et al., 2017) are ~96-99% H_2O, with the remaining few percent comprising of a mixture of H_2 (0.4-1.4%), CO_2 (0.3-0.8%), CH_4 (0.1-0.3%) and NH_3 (0.4-1.3%). From Earth-based telescopic observations, the surface of Enceladus is known to be rich in water ice (e.g. Grundy et al., 1999; Cruikshank et al., 2005; Emery et al., 2005), but the *Cassini* Visible-Infrared Mapping Spectrometer (VIMS) also identified CO_2 ice on the surface (Brown et al., 2006; Hansen and Romain, 2010), especially in the SPR. It is important to understand the distribution of CO_2 on Enceladus because of its association with and likely role in generating plume activity.

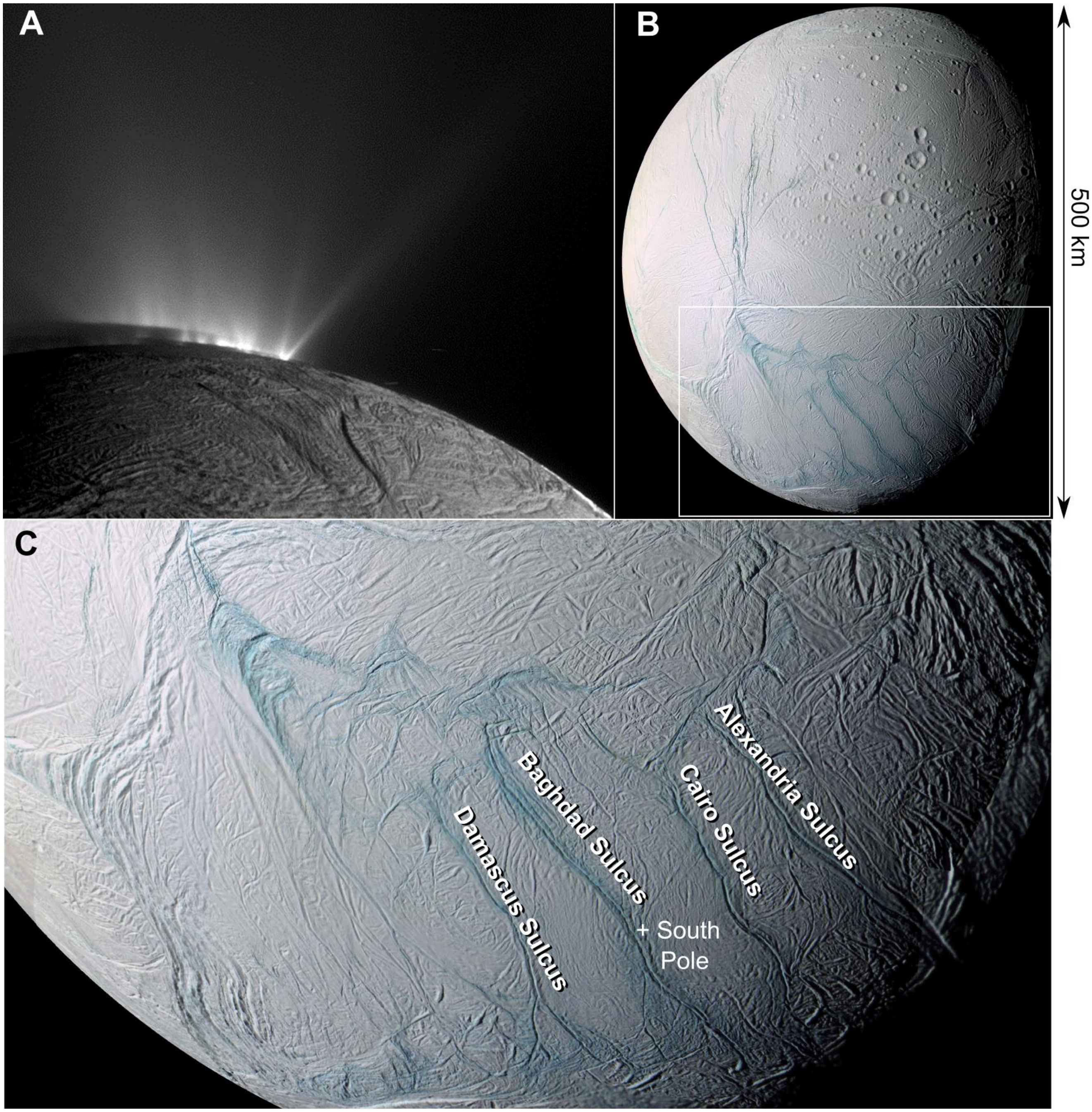

Fig. 1: Enceladus observed by the *Cassini* Imaging Science Subsystem (ISS) acquired on December 1, 2010. A – Plumes from the active faults in the South Polar region. B – Enhanced colors in the visible where the active faults appear in blue-green. C – Close-up view of the South Polar regions; the four active faults are labeled.

CO_2 is common in the outer Solar System and can exist as part of the body formation material; it can also be manufactured by chemistry using radiation or other energy sources (e.g., Hudson and Moore, 2001). CO_2 was found on the Galilean satellites by the *Galileo* Near Infrared Mapping Spectrometer (NIMS), apparently due to both interior outgassing (Carlson, 1999) and radiolysis (McCord et al., 1997; 1998), and also in a thin atmosphere around Callisto (Carlson, 1999). CO_2 was also detected on the Uranian satellites (Grundy et al., 2006; Cartwright et al., 2015) and Triton (e.g., Cruikshank et al., 1993; Holler et al., 2016).

CO_2 has been reported by VIMS on the surface of other icy Saturn satellites (e.g. Cruikshank et al., 2010; Filacchione et al., 2010). On Enceladus, CO_2 is likely part of the original condensates of the satellites of Saturn (McCord et al., 1998). CO_2 trapped in amorphous water ice below 120 K possibly formed in the outer regions of the solar nebula. Here, solid CO_2 in ice mixtures in molecular clouds at 10-30 K has been observed [De Graauw et al., 1996], also explaining its presence in comets and interstellar grains [e.g., Delsemme, 1982; Sandford and Allamandola, 1990; Whittet et al., 1996]. CO_2 also may be formed exogenically by irradiation of organic materials on the surface (Mennella et al., 2004), such as those found in carbonaceous chondrite meteorites (Carlson, 1999), or above the surface, in the plumes, although organics are not abundant in the plumes (Waite et al., 2017) or on the surface of Enceladus. Endogenically, CO_2 could exist as clathrates or dissolved in the Enceladus ocean water [e.g. Blake et al., 1991; Bouquet et al. 2015]. CO_2 is certainly being released in the plumes that emanate from the South Polar Region of Enceladus. Matson et al. (2012) proposed that the origin of the CO_2 was from degassing ocean water beneath the icy Enceladus crust. Due to the relatively high surface temperatures (100-140 K) of the South Polar Region [Spencer et al. 2006; Abramov and Spencer 2009; Taffin et al., 2012], CO_2 ice is not stable once exposed at the surface [McCord et al., 1998; Palmer and Brown, 2008]. However, CO_2 could be stable if trapped or complexed, such as in inclusions or clathrates [Brown et al., 2011]. Thus, any surficial CO_2 ice must be resupplied, and the form and abundance of the remaining CO_2 may be altered with time.

Near-infrared spectra of CO_2 (Fig. 2 and Fig. 3) exhibit a strong absorption band in the region 4.24-4.27 µm, due to the asymmetric stretching mode of the CO_2 molecule, and a weaker absorption near 2.7 µm (Fig. 4), due to $\nu 2+\nu 3$ vibration transition modes (e.g. Chaban et al., 2007). The longer wavelength absorption band position is sensitive to the nature and strength of molecular associations between CO_2 and its neighbors. Free CO_2 ice absorbs at 4.268 µm (Sandford and Allamandola, 1990). The difference between crystalline and amorphous CO_2 is small at VIMS spectral resolution, however the center position of the absorption band of amorphous CO_2 seem to be slightly shifted to longer wavelength compared to crystalline CO_2 (Fig. 2 and Fig. 3). Fig. 3 and Fig. 4 illustrate also that complexed CO_2 absorbs near 4.247 µm (Chaban et al., 2007), whereas CO_2 clathrate hydrates absorb between 4.28 µm and 4.30 µm (Oancea et al., 2012). This wavelength shift was observed, for example, for Callisto's surface (McCord et al., 1997, 1998).

Here, we investigate the presence, type and spatial distribution of CO_2 on Enceladus' surface using nine years of *Cassini* VIMS observations. We identify the forms of CO_2 present and their associations with surface features and phenomena, and thereby provide a basis for testing models of internal processes that may produce the plumes.

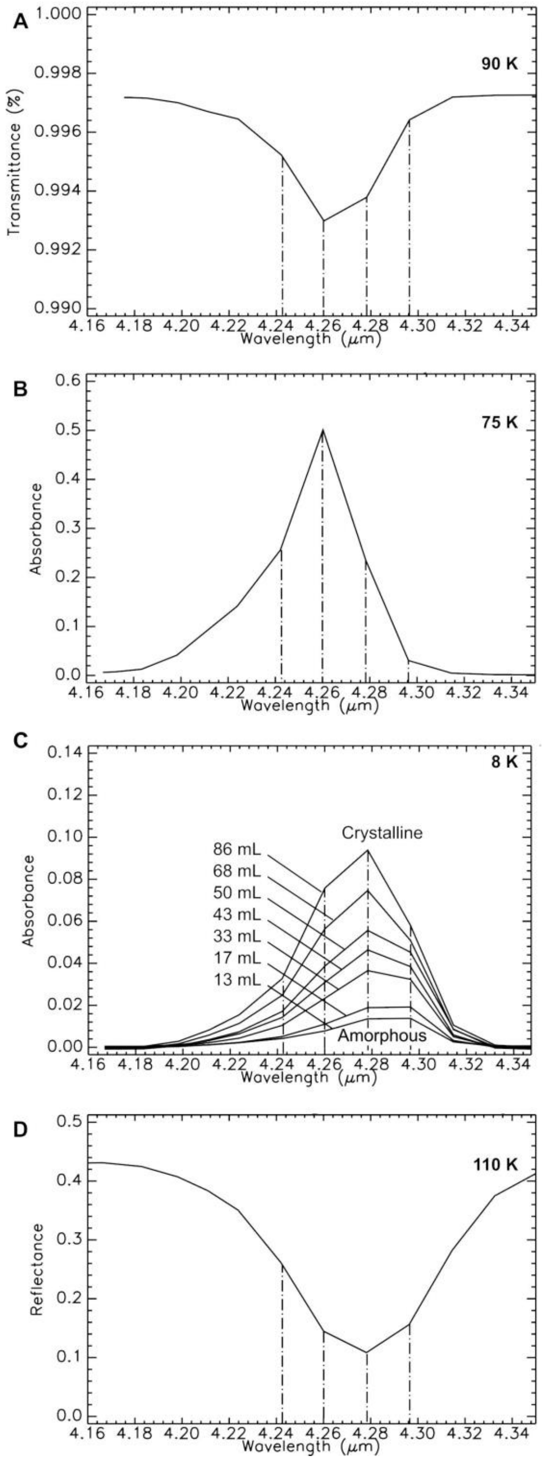

Fig. 2: Laboratory spectra of CO_2 resampled at VIMS wavelengths showing the absorption band position of the asymmetric stretching mode of the CO_2 molecule as a function of the type of the physical structure and type of bonds. (A) Complexed CO_2 at 90 K (Bernstein et al., 2005). (B) Crystalline CO_2 ice at 75 K (Isokoski et al., 2013). (C) Transition from CO_2 amorphous ice to CO_2 crystalline ice at 8 K (Escribano et al., 2013). (D) CO_2 clathrate hydrates at 110 K (Oancea et al., 2012).

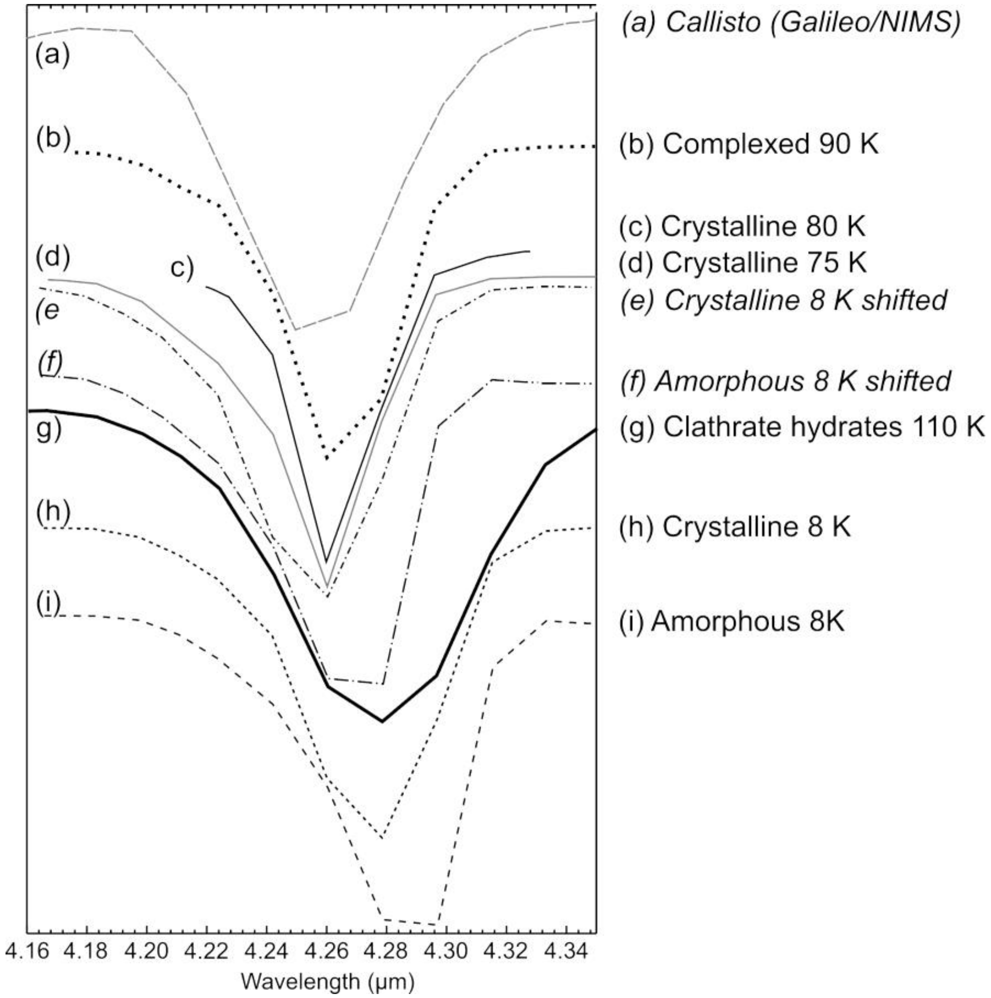

Fig. 3: Normalized spectra of CO_2–rich materials resampled at VIMS wavelengths showing the absorption band position variation of the asymmetric stretching mode of the CO_2 molecule. Labels in italics indicate spectra that are not from laboratory measurements or that are empirically shifted in wavelength to account for temperature effects. (a) CO_2-rich region on Jupiter's satellite Callisto measured by *Galileo* NIMS (McCord et al., 1998), and interpreted as complexed CO_2. (b) Complexed CO_2 at 90 K (Bernstein et al., 2005). (c) Crystalline CO_2 at 80 K (Escribano et al., 2013). (d) Crystalline CO_2 at 75 K (Isokoski et al., 2013). (e) Crystalline CO_2 at 8 K (Escribano et al., 2013), shifted towards shorter wavelengths to match the wavelength position of crystalline CO_2 (c) and (d) measured at higher temperatures[1]. (f) Amorphous CO_2 ice at 8 K (Escribano et al., 2013) shifted towards shorter wavelength by the same amount as (e) in order to account for the higher temperatures of the surface

---

[1] The shifted spectra Fig. 3e and Fig. 3f illustrate the theoretical position of the CO_2 absorption band depth of amorphous CO_2 at 75 or 80 K (between 4.26 and 4.28 µm) relevant for the surface of Enceladus. It is only theoretical because there is no spectrum of amorphous CO_2 ice available at the temperature of Enceladus. The only spectrum of amorphous CO_2 ice that we could find was acquired at 8 K (with an absorption centered between 4.28 and 4.30 µm), alongside a spectrum of crystalline CO_2 ice. Thus, the spectrum of crystalline CO_2 ice is used as a reference to prove that a temperature change from 8 K to 75 or 80 K shifts the CO_2 absorption band center of crystalline CO_2 ice from 4.28 to 4.26 µm. Assuming that for amorphous CO_2 ice a temperature increase from 8 K to 75 or 80 K results in the same shift of 0.02 µm in the absorption band center position as for crystalline CO_2 ice, the plot indicates that amorphous CO_2 is expected to have an absorption centered between 4.26 and 4.28 µm at 75 or 80 K instead of between 4.28 and 4.30 µm at 8 K.

of Enceladus¹. (g) CO_2 clathrate hydrates at 110 K (Oancea et al., 2012). (h) Crystalline CO_2 at 8 K (Escribano et al., 2013). (i) Amorphous CO_2 ice at 8 K (Escribano et al., 2013).

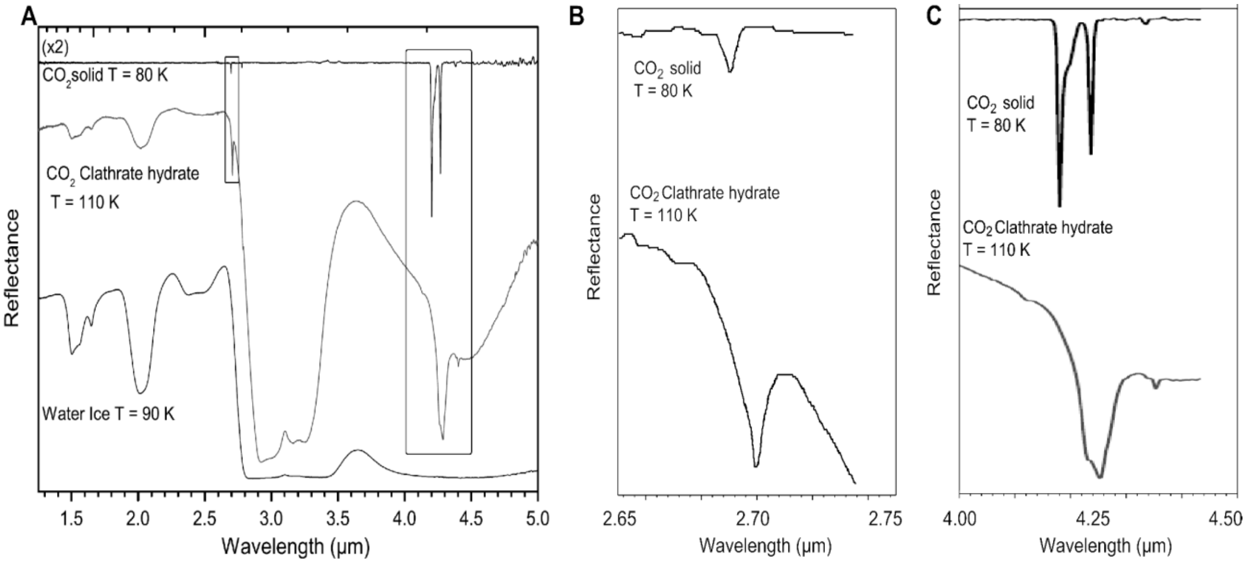

Fig. 4: High-resolution laboratory spectra of CO_2 ice and CO_2 clathrate hydrates by Oancea et al. (2012). A – General view. B – Close-up view of the 2.7 µm absorption band of CO_2. C – Close-up view of the 4.25 µm absorption bands of CO_2.

2. Spectral analysis of VIMS data to detect and map CO_2

2.1 Instrument specifications

VIMS (Brown et al. 2004), on board the *Cassini* spacecraft, observed the Saturn system between February 7, 2004 (orbit insertion occurred on July 1, 2004), and June 30, 2017 (Cassini dove into Saturn on September 15, 2017), according to archives on the Planetary Data System. For our analysis, we used 1760 VIMS observations from 31 *Cassini* Enceladus flybys (Table 1 in the Appendix). The infrared part of VIMS had a linear array detector: one exposure acquired data in whiskbroom mode for a single spatial pixel. From the dispersion of the image of this pixel on the focal plane, each detector received photons from the same field of view in a different contiguous waveband. The two-dimensional image of any scene was acquired sample by sample and line by line.

In the wavelength region of the CO_2 spectral features studied here (4.24–4.28 µm and 2.70 µm), VIMS data have a spectral sampling width of about 0.0166 ± 0.0006 µm. This spectral sampling is sufficient to detect all the CO_2 spectral features. However, VIMS spectra cannot resolve the CO_2 absorption band at 2.70 µm. Moreover, the band position shifts due to differences in molecule neighbor sites (e.g. complexed CO_2 vs. pure CO_2 ice, or CO_2 clathrate hydrates vs. crystalline CO_2 ice).

2.2 Calculation of CO_2 relative absorption band depths at 4.24-4.30 µm

One objective of this study is to characterize CO_2 absorptions bands (measurement of depth, width and position) on Enceladus. The focus of this section is to optimize the spectral analysis within a range of wavelengths that has a relatively low signal-to-noise ratio due to the broad and ubiquitous H_2O absorption band, the low solar flux of photons, and an instrument sensitivity near the edge of the detector that is less than in the center.

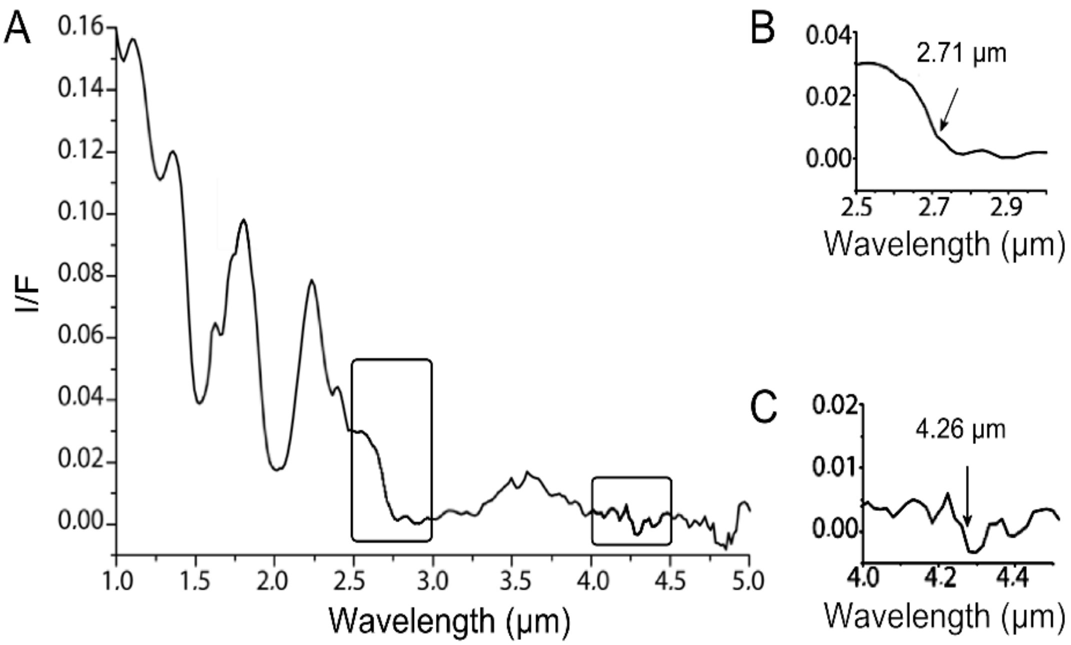

Fig. 5: VIMS average spectrum of the CO_2-rich part of the South Polar Region of Enceladus showing an absorption band at 4.26 µm and an inflection at 2.7 µm, both attributable to CO_2 (Oancea et al., 2012). A – General view, which indicates the low reflectance between 4.0 and 4.5 µm comparatively to wavelengths shorter than 2.5 µm, and the relative band depth of CO_2 compared to the H_2O ice absorption bands at 1.28, 1.5 2.0 and 3.0 µm. B – Close-up view of the 2.7 µm absorption band of CO_2. C – Close-up view of the 4.25 µm absorption band of CO_2.

2.2.1 Preliminary step: Scaling and ratioing of VIMS spectra

The stretching mode of the CO_2 molecule creates an absorption band in a range of wavelength that has a low solar photon flux and where the ubiquitous H_2O ice absorbs most of the remaining light. As a consequence, the signal-to-noise ratio in the spectra is never optimum for the measurement of CO_2 absorption bands and positions. In particular, any photometric effect of calibration artifact may have an amplitude that is comparable with the CO_2 absorptions. In order to minimize the uncontrolled variations of the spectra, we performed scaling and ratioing of VIMS spectra.

Scaling is the division of each spectrum by its median value in the intervals 4.0 µm and 5.12 µm. This range avoids the effects of large variations in the overtone absorption bands of H_2O ice and of the Fresnel peak of crystalline H_2O ice that occur at shorter wavelengths. Therefore, the median value over this entire range of wavelengths is less sensitive to noise in the data than the value at one given wavelength. This is a common way to minimize the effects of albedo, illumination variations and possible remaining systematic calibration artifacts.

Ratioing is the division of each scaled VIMS spectrum by the average scaled spectrum of Enceladus. This processing step is a way to minimize the effects of mixture of local components (here, CO_2 materials) with the average surface composition, which is mostly H_2O ice. Since the surface composition of Enceladus is very homogenous and is globally dominated by H_2O ice, and since plume fallout add fresh H_2O ice deposits that may mix with any CO_2 component, all VIMS spectra have deep and broad spectral features of H_2O. After ratioing, the absorption bands of the local component are more likely to be detected by the calculation of a simple band depth parameter. This preparation step was successfully applied on spectra of Ceres by the Visible and InfraRed mapping spectrometer (VIR) of Dawn mission for the search of H_2O ice (Combe et al., 2016; 2018).

2.2.2 Calculation of CO_2 band depths that vary in position between 4.24 and 4.30 µm

Free CO_2 ice and complexed CO_2 may be mixed within a VIMS pixel: the expected CO_2 absorptions may vary in width and in center position between 4.24 and 4.30 µm. When only one form of CO_2 is present, the absorption band is narrow enough that it only involves one VIMS wavelength channel (Fig. 5). On the other hand, when mixtures occur, up to four VIMS wavelength channels may be within the CO_2 absorption band, as illustrated in Fig. 4. The absorption band depth is calculated using the average of three channels between 4.18 and 4.22 µm and three channels between 4.32 and 4.36 µm, so as to define the shoulders of the absorption. This operation minimizes the effects of illumination and albedo variations, and the average value over three VIMS wavelength channels is less sensitive to random noise in the data or occasional spikes in the spectra than the pixel value taken at a single wavelength. In order to calculate the CO_2 absorptions band depths, we used VIMS wavelength channels centered at 4.24, 4.26, 4.28 and 4.30 µm.

Any possible detection of any CO_2 absorption band has to meet the following criteria: 1) a detection threshold is set to equal the standard deviation of the absorption band depth values, and 2) the pixels that meet the detection criterion must define spatially-coherent areas (i.e. several contiguous pixels). When values lower than one occur at more than one VIMS wavelength channel (4.24, 4.26, 4.28 and 4.30 µm), this is interpreted as mixture of CO_2 compounds that may include complexed CO_2, CO_2 ice and CO_2 clathrate hydrates.

2.3 Calculation of an inflection at 2.7 µm caused by a CO_2 absorption

All forms of solid CO_2 have a narrow absorption band at 2.7 µm (Fig. 4A). At VIMS spectral resolution and sampling, this theoretically creates an inflection in the spectra (Fig. 4B). Since the 2.7µm absorption of CO_2 is weak and not fully resolved by VIMS, we cannot use the calculation of a 2.7µm absorption band depth to quantify the CO_2. However, at this wavelength, the solar flux is one order of magnitude higher than at 4.26 µm, which is adequate to make use of this band as a detection criterion. This inflection, therefore, can be measured using a traditional absorption band depth calculation (Clark and Roush, 1984), assuming a linear continuum between surrounding wavelength channels.

2.4 Optimization procedure of the signal-to-noise ratio with VIMS data

CO_2 absorption bands at 4.24-4.28 µm are faint and their variations are close to the instrument detection limit. Since the signal-to-noise ratio of VIMS spectra is the main challenge to study absorption bands of CO_2, we made an optimization in four steps:

1- Selecting VIMS pixels that cover less than 20 km^2 (the area covered by each pixel is calculated from the pixel corner coordinates)
2- Selecting VIMS images based on the spectral signal-to-noise ratio (measured by the standard deviation of the dark current)
3- Projecting and spatially merging VIMS data that meet the two quality criteria (points 1 and 2) where the main faults on Enceladus are spatially resolved.
4- Binning all VIMS observations with a spatial sampling of 4.4 km× 4.4 km (19.36 km2, or 1° per pixel)in order to increase the signal-to-noise ratio of VIMS spectra.

3. Results: Distribution and nature of CO_2 deposits on Enceladus

3.1 Deeper CO_2 absorption bands in the South Polar Region

3.1.1 Comparison of absorption band distributions at 2.70 µm and 4.24-4.30 µm

Fig. 6 shows maps of Enceladus from the *Cassini* mission in cylindrical and polar projections. Fig. 6A is a contextual color mosaic of ISS images in the visible. Fig. 6B shows the coverage of VIMS data used in this analysis. In order to maximize the signal-to-noise ratio, multiple observations of an area are combined. As a consequence, the maps of CO_2 absorption band depth are more reliable where the number of observations is high. The highest redundancy of VIMS observation occurs on the area between 110°W and 20°W and between -70° and +70° in latitude. The North Polar Region has the smallest number of observations. In first order, mapping of CO_2-rich compounds is estimated by the absorption band depth between 4.24 and 4.30 μm (Fig. 6C). Measurements of high values of the CO_2 absorption band depth that correspond to the most spatially-coherent area (no gap in the detection and well-defined contours) occur near the South Pole. High values in the northern hemisphere around 60°N, 270°W, as well as around the North Pole between 70°N and 80°N correspond to a small (<20) number of observations. At mid-latitudes (between 60°S and 60°N), low values (<0.1) cover a large between 120°W and 300°W, whereas moderately low values (0.1-0.2) cover an equally large area on the opposite hemisphere. In general, when detected values are low (<0.05), or result from a low number of observations (<10), they have to be interpreted with caution.

For the 2.70 μm absorption (Fig. 6D), the highest values that cover a spatially-coherent area are also observed in the South Polar Region, similar to the 4.24-4.30 μm absorption. The maximum value is measured on the fault that forms the base of the Tiger Stripes and connects them perpendicularly on the upper half of the polar view. High values are also measured in the northern hemisphere between 270°W and 330°W, but not around 240°W, which is spectrally different from the 4.24-4.28 μm absorption.

The fact that the distribution of absorption bands at 2.70 μm and at 4.24-4.30 μm present the most obvious similarities over the South Polar Region is an indication that they are both sensitive to the same surface component (CO_2). Because the 2.70 μm absorption in VIMS spectra appears only as an inflection in a range of wavelengths that is sensitive to broad and strong absorption processes, the observed variations of the 2.70 μm absorption band depth cannot be interpreted alone for quantifying CO_2.

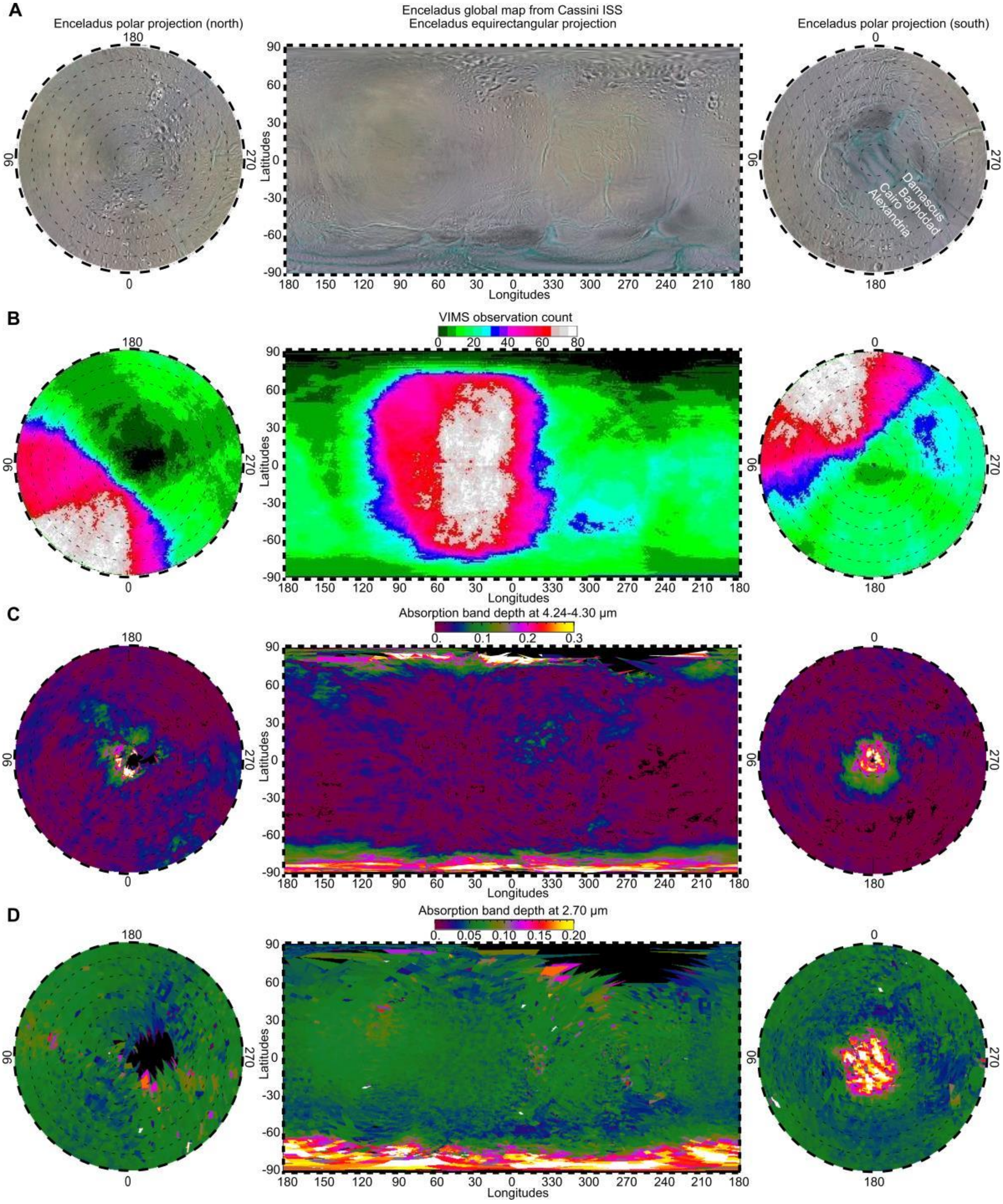
A
Enceladus polar projection (north)
Enceladus global map from Cassini ISS
Enceladus equirectangular projection
Enceladus polar projection (south)
Damascus
Baghdad
Cairo
Alexandria
B
VIMS observation count
0 20 40 60 80
C
Absorption band depth at 4.24-4.30 µm
0. 0.1 0.2 0.3
D
Absorption band depth at 2.70 µm
0. 0.05 0.10 0.15 0.20
Latitudes
90 60 30 0 -30 -60 -90
Longitudes
180 150 120 90 60 30 0 330 300 270 240 210 180
180 90 270 0

Fig. 6: Enceladus global and polar maps calculated with data from the entire Cassini mission. The leading hemisphere (centered on 90°W) is on the left side of each map, whereas the trailing hemisphere (centered on 270 °W) is on the right. The polar projections extend from the pole to 20° latitude. (A) ISS color mosaic. The four major faults of the South Polar Region are labeled. (B) Count of VIMS observations of the surface of Enceladus with spatial resolution better than or equal to 5 km/pixel for the entire *Cassini* mission up to March 2016. Most areas have been observed multiple times, except the North Polar Region. (C) Combined CO_2 absorptions between 4.24 and 4.30 µm. It is an intermediate step in the making of the CO_2 distribution maps shown in Fig. 7. The median value of all VIMS observations is displayed where data overlap. (D) Inflection at 2.70 µm in VIMS spectra, calculated as an absorption band depth. The highest resolution observations are displayed on top of the map.

3.1.2 Combined analysis of the absorption bands at 2.70 µm and 4.24-4.30 µm

In this part of the study, the 2.70 µm absorption band depth is a conditional criterion for the detection of any form of surficial CO_2. The rationale behind this assumption is that the 2.70 µm absorption band should always exist in a CO_2-rich material. In particular, on the South Polar region, where several studies have confirmed CO_2 ice deposits (Brown et al., 2006; Palmer and Brown, 2008; Brown et al., 2011) both absorption bands are strong. According to laboratory experiments, although the stretching mode of the CO_2 molecule produces a much stronger absorption band at 4.24-4.30 µm than the vibration transition mode at 2.70 µm, the 2.70 µm absorption band exists regardless of the physical structure of CO_2, whether it is crystalline CO_2 ice (Isokoski et al., 2013), complexed CO_2 (Bernstein et al., 2005) or CO_2 clathrate hydrate (Oancea et al., 2012). Furthermore the absorption feature is theoretically observable at VIMS spectral resolution (Oancea et al., 2012). We did not find measurements or documentation for amorphous CO_2 ice (Escribano et al., 2013 provide only spectra for the stretching mode). In addition, minerals that exhibits an absorption band near 4.25 µm such as beryl and cordierite (McCord et al., 1998; Clark et al., 2003) have also an absorption feature near 2.70 µm.

The combined detection of an absorption between 4.24 and 4.30 µm and an inflection at 2.70 µm is mapped in Fig. 7. In this map, the absence of a 2.70 µm absorption band is used as a mask on the map of the 4.24-4.30 µm absorptions.

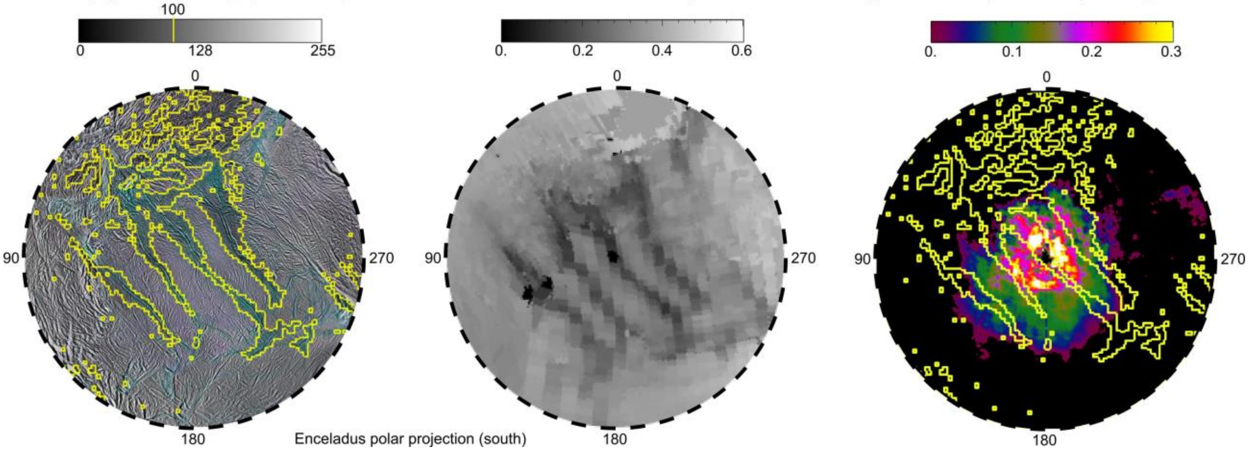

Fig. 7: Maps of Enceladus obtained from *Cassini* observations in southern polar projection between 50°S and 90°S. (A) Surface albedo as observed by ISS in the visible. Yellow contour lines indicate contrast in brightness in the ISS blue channel between the Tiger Stripes (blueish) and the surrounding terrains (gray). (B) Surface reflectance as observed by VIMS at 2.3 µm. The highest resolution observations are displayed on top of the map. (C) Consolidated map of CO_2 absorption bands on Enceladus. The median value of all VIMS observations is displayed where data overlap. The presence

of CO_2 is confirmed only where both 2.70 µm absorption band depth and 4.24–4.30 µm absorption band depth are greater than 0.07. The other regions of Enceladus are not shown here because the maps would be entirely black.

3.2 How to reconcile results from absorption features at 4.24-4.30 µm and 2.70 µm in VIMS spectra of Enceladus

In section 3.1, maps of the CO_2 absorption band depth at 4.24-4.30 µm and 2.70 µm indicate different distributions across the surface of Enceladus. Although the inflexion at 2.70 µm is detected in most VIMS spectra, the South Polar Region above 70°N is the only location where it reaches a maximum (>0.12). In contrast, the absorption band at 4.24-4.30 µm has several maxima in the northern hemisphere, above 50°N and in the South Polar Region below 70°S. At this point of the analysis, the question is whether the two absorption features indicate contradictory results or if they complement each other.

3.2.1 Arguments in favor of interpreting any absorption feature at 4.24-4.30 µm as evidence for CO_2

- In laboratory spectra of CO_2-rich materials, the transition vibration absorption of CO_2 at 2.70 µm is always weak and not spectrally resolved by VIMS.
- Although the absorption band depth at 4.24-4.30 µm and 2.70 µm are correlated in the South Polar Region of Enceladus, many VIMS spectra of the northern hemisphere exhibit only a strong absorption feature at 4.24-4.30 µm and a weak one at 2.70 µm, which indicates that the two types of absorption are not always correlated.
- CO_2 is known to be present at the surface and in the plumes that result from eruptions on the active faults of the South Polar Region.

3.2.2 Arguments in favor of a detection of CO_2 only when both absorption features at 4.24-4.30 µm and 2.70 µm are present

- All laboratory measurements of any form of CO_2 (crystalline ice, complexed and clathrate hydrates) and of CO_2 inclusions in minerals (McCord et al., 1998; Clark et al., 2003) such as beryl (Wood and Nassau, 1967) and cordierite (Farrell and Newnham, 1967) confirm the presence of the two absorption bands.
- From laboratory experiments, the presence of a strong 4.24-4.30 µm CO_2 absorption band means that a strong 2.70 micron band is systematically present.
- A few minerals have an absorption band 4.24-4.30 µm that is not related to CO_2such as hydroxyl-apatite and hydroxyl-goethite (McCord et al., 1998; Clark et al., 2003), thus any other absorption feature that is known to be present in CO_2-rich materials, such as the 2.70 µm absorption band, should be used as an additional detection criterion.

3.2.3 Synthesis: absorption features at 4.24-4.30 µm and 2.70 µm may be sensitive to different forms of CO_2

The two subsections above show that ignoring the 2.70 µm absorption (subsection 3.2.1) or combining absorption features at 4.24-4.30 µm and 2.70 (subsection 3.2.2) both result in contractions that are difficult to justify about CO_2 spectra. In order to reconcile the two results, we adopt the hypothesis that the two CO_2 absorption features do not carry the same type of information, resulting in non-correlated variations of the absorption band depths. This assumption implies that the inflexion at 2.70 µm cannot be ignored, but that it should not be used as the sole detection criterion for CO_2 or as a parameter for CO_2 abundance estimates. Subsequently, Fig. 7 may just illustrate the distribution of one form of CO_2 compound, which is characterized by strong absorptions at 4.24-4.30 µm and at

2.70 μm, and that is may not be representative of other forms of CO_2 compounds. The analysis of absorption band position may help clarify this assumption and determine whether the distribution of various types of CO_2 is consistent with the differences observed between the absorption band depths at 4.24-4.30 μm and 2.70 μm.

3.3 Variations of the CO_2 absorption band shape and position

One objective of this study is to discriminate between various types of CO_2 compounds (Fig. 8 and Fig. 9) by analyzing the absorption band depth measured at the expected position for free, amorphous CO_2 ice (4.28 μm, Fig. 8A and Fig. 9C), crystalline CO_2 ice (4.26 μm, Fig. 8B and Fig. 9B), CO2 clathrate hydrates (and Fig. 9D) and complexed CO_2 (4.24 μm, Fig. 8C and Fig. 9A). A broad band that covers more than one VIMS channel (Fig. 8D and Fig. 9E-J) represents either a mixture of various CO_2-rich compounds , or large grain sizes.

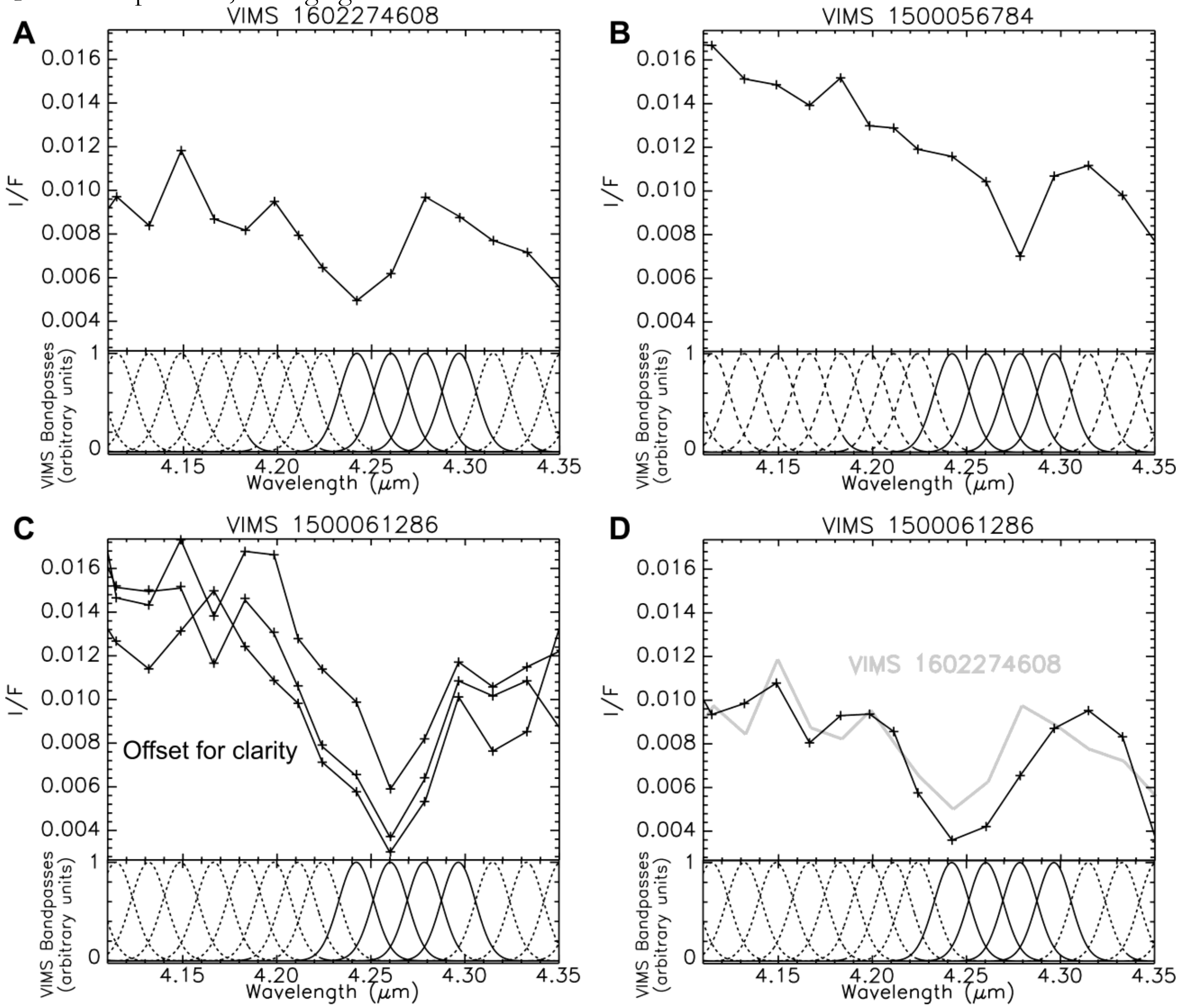

Fig. 8: Example of VIMS spectra showing CO_2 absorption bands of various shapes and positions, as expected for deposits of complexed CO_2 (A), free CO_2 ice (B), and combinations of the two (C and D). The three solid line Gaussian curves correspond to the VIMS bandpasses that are used to measure the CO_2 absorptions. The number above each plot indicate the VIMS file.

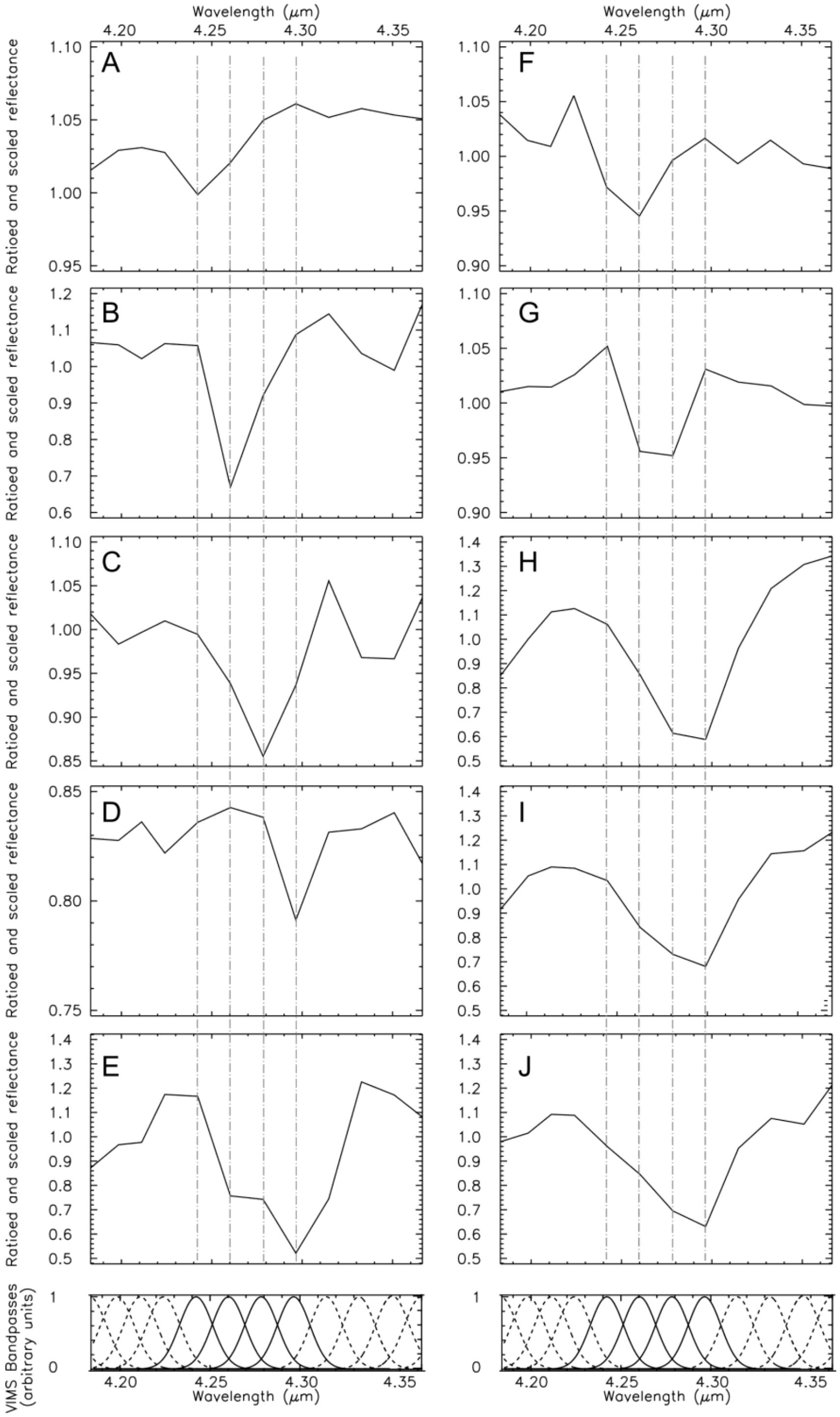

Fig. 9 Example of VIMS spectra that are averaged over multiple observations, scaled and ratioed (for details, see text in section 2.2.1) in order to enhance the CO_2 absorption bands. Uncertainties are estimated to be on the order of ±0.01. Various shapes and positions of the CO_2 absorption bands are observed, as expected for deposits of complexed CO_2 (A), free CO_2 ice (B), possible amorphous ice (C) and possible CO_2 clathrate hydrates (D). Combinations of two or more types of CO_2 components may create absorption features with more than one minimum (E). Several types of CO_2 components, or rain size variations or temperature variations may create broad bands and different wavelength position of the band center (F-J) The Gaussian curves correspond to the VIMS bandpasses.

3.3.1 Comparative absorption band depth distributions at 4.24, 4.26, 4.28 and 4.30 µm

Although laboratory experiments show no evidence that the stretching mode absorption band of the CO_2 molecule at 4.24-4.30 µm could exist without the vibration transition mode at 2.70 µm, a large number of VIMS spectra of Enceladus show a strong absorption at 4.24-4.30 µm (>0.3) and a weak (<0.07) absorption feature at 2.70 µm. In Fig. 10A-D, we present the global distributions of absorption band depths measured at four consecutive VIMS wavelength channels (in increasing order), which are all sensitive to CO_2.

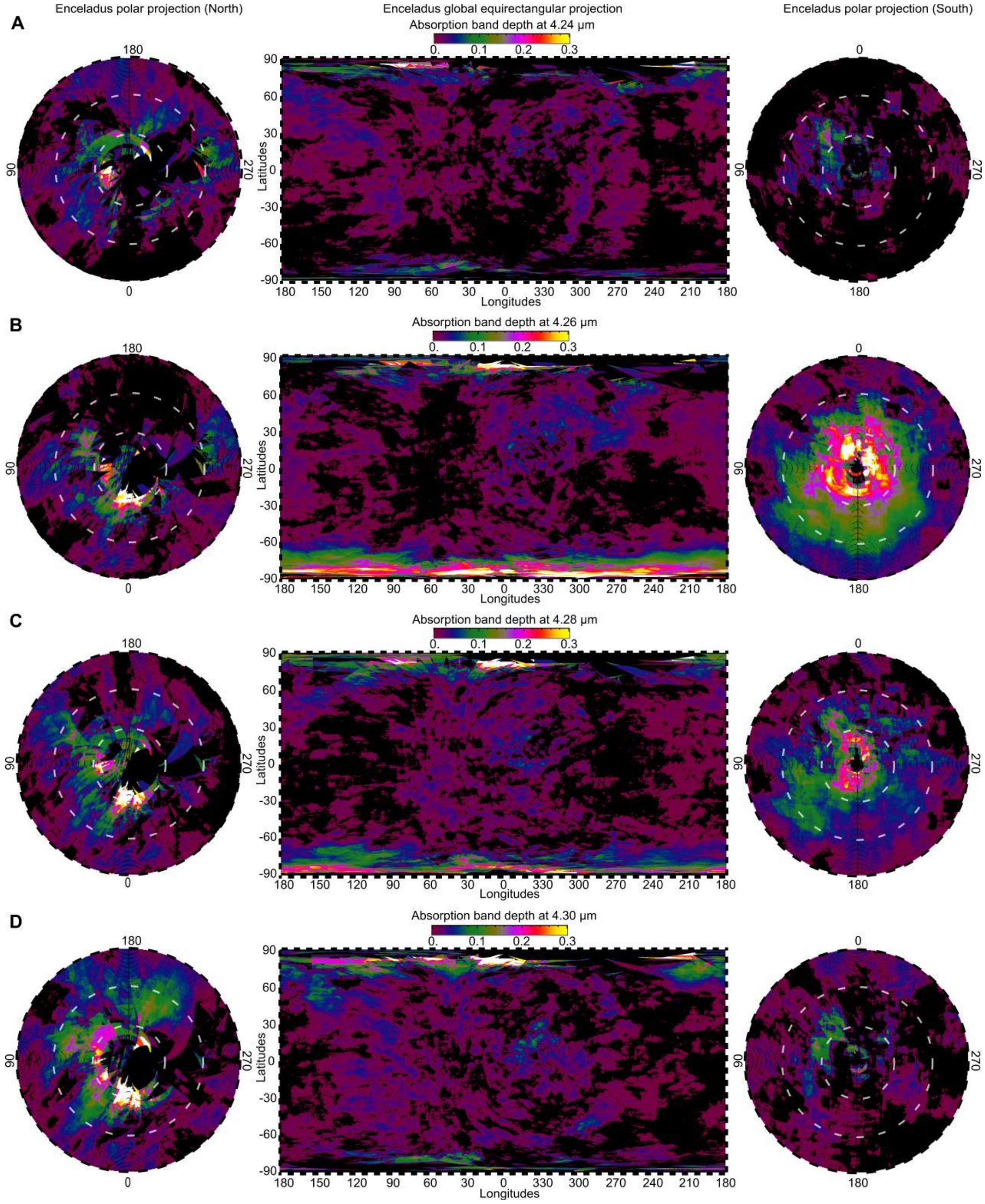

Fig. 10: Maps of the CO_2 absorption band depth on the South Polar Region of Enceladus from 60°S to 90°S. The median value of all VIMS observations is displayed where data overlap. From top to bottom, the spectral parameters represent absorptions at 4.24 µm (A), 4.26 µm (B), 4.28 µm (C), and 4.30 µm (D) respectively.

Over the South Polar Region (60°S-90°S), the absorption band measured at 4.26 µm (Fig. 10B) is clearly the strongest of all. At this wavelength, high values (>0.2) represent a larger area than the band depth measured at other wavelengths. In addition, these high absorption band depth values at 4.26 µm occur mostly, between 70°S and the South Pole, whereas the absorption band depth measured at other wavelength have mostly moderate values (<0.1) in that region. In all four maps of absorption band depths, several areas with values ~0.3 exist in the North Polar Region around 80°N between 0° and 90°W.

3.3.2 Position of the asymmetric stretching mode absorption maxima of the CO_2 molecule

In order to determine the nature of the CO_2 detected on the surface, we performed an analysis of the absorption band position of the CO_2 molecule stretching mode. As shown in Fig. 8, this absorption band may exhibit one or two absorption maxima, which likely indicates a possible mixture of CO_2-rich compounds rather than a homogenous composition. Ideally, the analysis of the absorption band position would be performed by fitting one or more Gaussian curves to the CO_2 absorption feature as a way to achieve accurate measurements. However, since the number of VIMS wavelength channels between 4.24 and 4.30 µm is only four, the fitting of two or more Gaussian curves is an under-determined problem (with more unknowns than equations). As a consequence, the absorption band analysis is limited to measurements of absorption band depths, position of the absorption maximum (or maxima when two peaks are detected), and absorption band area.

Fig. 11 combines the information of the multiple peak position with the absorption band area. Peaks at all wavelengths between 4.24 and 4.30 µm are observed globally on Enceladus, and all combinations of two peaks (4.24 µm and 4.28 µm, or 4.24 µm and 4.30 µm, or 4.26 µm and 4.30 µm) are also observed. Most of Enceladus' South Polar Region between 70°S and 90°S is characterized by an absorption band with a maximum centered at 4.26 µm (green) that is characteristic of crystalline CO_2 ice. The North Polar Region exhibits several homogenous large areas near 80°N with strong, absorptions at 4.30 µm (white) that may indicate CO_2 clathrate hydrates. Overall, the occurrence of maximal absorptions at 4.26 µm and 4.30 µm correspond to the largest spatially-coherent zones on Enceladus. In the North Polar Region, few, small areas show a strong double-peak absorption at 4.26 and 4.30 µm (magenta) which may indicate crystalline CO_2 ice and CO_2 clathrate hydrates,, and at 4.24 and 4.28 µm (cyan), which may indicate complex CO_2 and possibly CO_2 clathrate hydrates or CO_2 ice. At latitudes below 70° in both hemisphere, the values of the absorption band depth are <0.07, which indicate a low probability of detection.

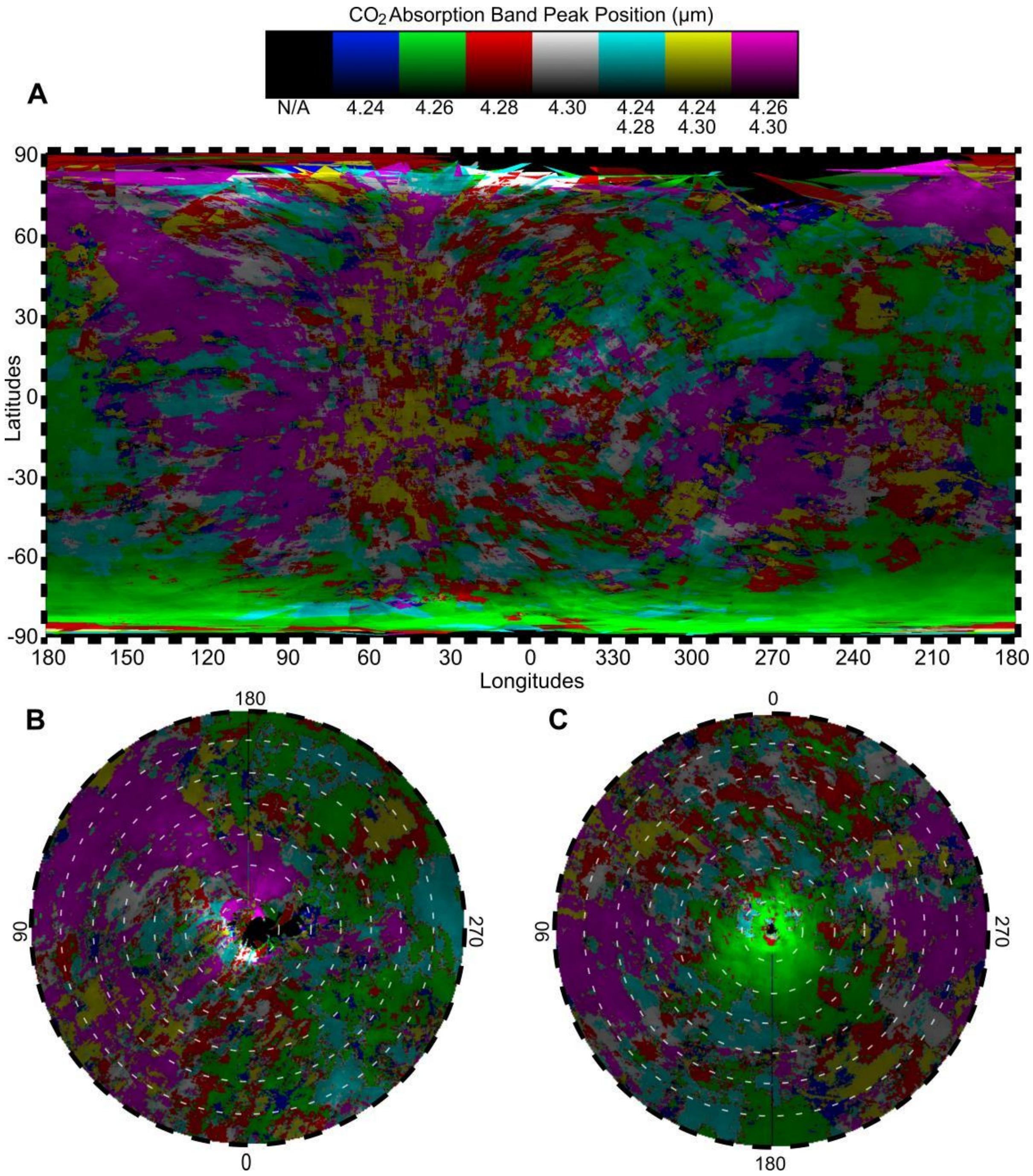

Fig. 11: Wavelength position of the CO_2 absorption local maxima between 4.24 and 4.30 µm. The hue illustrates the position, and the brightness is sensitive to the absorption band area (brighter means a larger area). (A) Global map in equirectangular projection. (B) Polar map between 20°N and 90°N. (C) Polar map between 20°S and 90°S.

3.3.3 Sensitivity of absorption band position to the type of CO_2

In the spectra of many minerals and ices (e.g. H_2O), the position of absorption bands shifts as a function of temperature. On Enceladus, variations of >100 K in the surface temperature are inferred from *Cassini* Composite Infrared Spectrometer (CIRS) measurements on the Tiger Stripes and between them [Abramov and Spencer, 2009; Goguen et al., 2013]. In VIMS spectra of Enceladus, there is no apparent correlation between the high temperature of the main active faults and the position of the CO_2 absorption bands between 4.24 and 4.30 µm. As a result, the wavelength shift observed on Enceladus must be caused by mixture in a chemical compound [Mastrapa et al., 2005].

3.3.4 Result summary: Nature and distribution of CO_2 on Enceladus

Although most of Enceladus surface exhibits spectral features at 2.7 µm and in the range 4.24-4.30 µm, the relative strengths of these two absorption bands may be sensitive to the different states of CO_2 exposed. According to laboratory measurements, measurements of the absorption band position between 4.24 and 4.30 µm help determine whether CO_2 samples are predominantly free, complexed (Chaban et al., 2007) or present as CO2 clathrate hydrates (Oancea et al., 2012). In our maps of Enceladus, we observe variations in absorption band position, similar to observations on Callisto (McCord et al., 1997, 1998) or Ganymede, that are consistent with the presence of CO_2 ice and complexed CO_2, , and possible CO_2 clathrate hydrates. Mixture of CO_2 ice, complexed CO_2, and CO_2 clathrate hydrates likely explains the observed lateral variations of the CO_2 absorption band width on Enceladus. Even though the grain size distribution and surface temperatures may also affect the CO_2 absorption band width in some extent, the effects are not as strong, and thus less likely to be measured by VIMS. As illustrated in Fig. 7D, the combination of absorption bands of crystalline CO_2 ice, amorphous CO_2 ice, complexed CO_2 and CO_2 clathrate hydrates may produce a single, wide absorption. On first order, from our analysis, four main types of compositional units can be identified globally:

- A strong absorption band at 2.7 µm is found exclusively on the South Polar Region delimited by the Tiger Stripes, and it is associated with a strong absorption band centered at 4.26 µm, characteristic of crystalline CO_2 ice. The deepest absorption bands at 4.26 µm occur between the main active faults, although the correlation is not very clear.
- A weak or moderate absorption band at 2.7 µm and a strong absorption which may occur anywhere in the range 4.26-4.30 µm may be due to CO_2 clathrate hydrates, and occur on the North Polar Region only.
- Moderate absorption bands at 2.7 µm and in the range 4.24-4.30 µm are measured at mid-latitudes (60°S-60°N) on the anti-Saturn side (300°W-120°W). The high variability in the position of the absorption stretching mode of the CO_2 molecule in that region suggest mixtures of different CO_2 compounds on the surface.
- Weak absorption bands at 2.7 and 4.26 µm are measured at mid-latitudes (60°S-60°N) on the sub-Saturn side (120°W-300°W). Although the absorption band depths are close to the noise level in the spectra, they may be sensitive to small amounts of crystalline CO_2 ice on the surface.

4. Interpretation: sources and transport of CO_2 on Enceladus

The presence and distribution of one or several forms of CO_2 is relevant to the interpretation of geophysical processes that occur on Enceladus and the possible interactions with the specific environment created by the vicinity of Saturn, such as the magnetic field. Maps of the three absorption bands of CO_2 on Enceladus support two main results.

First, the distribution of CO_2 can help identify its origin. In order to interpret the origin of surface materials on Enceladus, three hypotheses may be considered: endogenic (i.e. release by venting through the crust), exogenic (i.e. delivery by collision with a CO_2-rich object), and in-situ (i.e. formation by chemical reaction or parent molecules and particles).

Second, the different forms of CO_2 detected on the surface may have implications for the formation, transport and deposition mechanisms for this constituent. As a follow-up of section 3.2.3, we observed that where the 2.7 µm band is mostly correlated with the 4.26 µm band, which is consistent with a higher abundance of free CO_2 ice. In locations where the 4.24-4.30 µm band is present, but the 2.7 µm band is weak or absent, other CO_2 compounds are more abundant. In particular, the fact that the 4.30 µm sensitive to CO_2clathrate hydrates is strong on the northern polar region is consistent with a more stable storage of CO_2 at Enceladus northern polar latitudes than on the South Polar Region. As a corollary, the strong 4.26 µm band around the south pole indicates greater recent exposure of the less stable free CO_2 ice at Enceladus, along the Tiger Stripes.

4.1 CO_2 ice on the South Polar Region could be from local sources

Absorption bands of CO_2 measured by VIMS are stronger in a zone that includes the main active faults. Both higher abundances and larger grain sizes may produce deeper absorptions, whereas larger grains may also cause wider absorption bands. With CO_2, there is no known way to evaluate the relative role of abundance vs. grain size from near-infrared absorption bands alone because the absorption bands are too narrow for a reliable analysis of bandwidth (they are not spectrally resolved by VIMS). In the following subsections, we assume that the observed absorption band depths are mostly sensitive to the abundance of CO_2.

4.1.1 Crystalline CO_2 ice on the main active faults region: In situ deposition of CO_2 from gas pockets

The strongest detection of exposed CO_2 on the surface of Enceladus is observed in the South Polar Region, within the limits of the main active faults (the Tiger Stripes), which indicates that tectonic activity has some control on the release of CO_2, and therefore suggesting a source at the surface connected to an internal reservoir.

When endogenic materials reach the surface of a planet, the highest concentrations might be expected, intuitively, to be found near the source, and with concentrations decreasing as function of distance from the points of origin. The distribution observed in VIMS data is consistent with release of CO_2 from gas pockets between the faults that host plume eruptions [Matson et al., 2018]. The presence of CO_2 ice and possible CO_2 clathrate hydrates is compatible with the gas pocket model: gas seeping may deliver pure, cold CO_2 at low velocity, whereas blow-out eruption of gas pockets may vent both pure CO_2 (most of which would escape) and CO_2 clathrate hydrates.

CO_2 ice deposits may come from seeping of CO_2 gas through narrow fractures

Pure CO_2 gas can be released by seeping through a narrow fissure that connects to a gas pocket between the internal ocean and the H_2O ice crust, between the main active faults [Matson et al., 2018]. During its seep through the ice its temperature is reduced. By the time it exits, it is in the range of ~70 to ~119 K. This constrains the deposition of CO_2 adjacent to the nozzle of the fissure, and there is relatively little transport of CO_2 away from these vents.

Plumes, on the other hand, release primarily H_2O and a fraction of a percent of CO_2 at speeds that exceed the escape velocity for Enceladus. For these reasons, the detection of pure CO_2 ice strongly supports the gas pocket model. Any deposit of amorphous CO_2 ice may crystallize eventually. On surfaces where the temperature exceeds 120 K, CO_2 ice sublimates rapidly over geologically-relevant timescales [James et al., 1992]; consequently, observation of CO_2 ice on Enceladus implies a recent deposition, which is consistent with contemporary activity.

4.1.2 Deeper CO_2 absorption bands between the Tiger Stripes: Possible role of H_2O and surface temperature

Because plume eruptions on the Tiger Stripes are one source of CO_2 (Waite et al., 2006) mixed with H_2O (dominant) and other minor species, they may produce deposits where CO_2 is mixed as well. Gas seeping through the ice lid (Matson et al., 2018) are sources of pure CO_2, distinct from the Tiger Stripes. The concentration of CO_2 in the deposits from gas seeping is expected to decrease as a function of the distance from their source. This may explain why the highest concentrations of CO_2 ice (Fig. 7) may not be located near the Tiger Stripes.

Partial masking of surface CO_2 by more recent H_2O deposits

Absorption bands of H_2O at 1.5 and 2 µm are ~25% stronger on the Tiger Stripes (e.g. Jaumann et al., 2008; Scipioni et al., 2017) than in between. In addition, H_2O absorption bands are very deep everywhere on Enceladus (between 42 and 75% of the signal at 1.5 µm, according to Jaumann et al., 2008), including where CO_2 is the most abundant (Brown et al., 2006). Changes in the depth and width of the H_2O absorption bands, as well as the strength of the Fresnel peak of H_2O ice at 3.1 microns are interpreted as variations of grain sizes (Jaumann et al., 2008; Taffin et al., 2012; Scipioni et al., 2017) and surface temperature (Taffin et al., 2012). In all these studies, the hypothesis for possible variation in H_2O abundance across the South Polar Region is never considered. However, assuming the distribution of the H_2O absorption band depth is representative of the abundance of H_2O at the surface, its anti-correlation with CO_2 band depth favors the hypothesis of independent events, implying that the CO_2-rich units are not likely plume fallout.

H_2O-rich plume eruptions on Enceladus have been observed multiple times by *Cassini* (Hansen et al., 2006); CO_2 has been detected also in smaller proportions (Waite et al., 2006). To date, however, eruptions or releases of pure CO_2 have not been observed. As a consequence, if H_2O-rich eruptions are more frequent or have more discharge than CO_2-rich venting, H_2O deposits on the surface of active faults may partially mask deposits of CO_2.

Local CO_2 abundance variations controlled by surface temperature heterogeneities

Variations of the CO_2 absorption band depth over a given type of terrain (on or in between the main active faults) can be also controlled by the local surface temperature. Although on average the Tiger Stripes are warmer than the intermediate terrains, the internal convection in the ocean may create temperature variations at the surface of the ocean [Stegman et al., 2009] that can be transmitted by conduction at the surface of the faults or at the surface of the thick crust [Ingersoll and Pankine, 2010]. Furthermore, active convection may also erode the thickness of the ice lid or crust and allow more heat to be conducted through the ice. As a consequence, surface temperature variations in the faults or in between may lead to sublimation, transport and condensation of CO_2. This mechanism may reinforce the anti-correlation of CO_2 abundance with the Tiger Stripes.

From *Cassini* CIRS observations acquired on July 14, 2005 at ~25 km/pixel, the temperature over the average polar region southern of 65°S was ~133 ±12 K whereas the average over the Tiger Stripes was 145 ±14K [Spencer et al. 2006, Abramov and Spencer, 2009]. Bright 16 - 200 µm emission at the anti-Saturn end of Damascus and Baghdad Sulci may indicate excess endogenic power, either from the Tiger Stripes or the inter-stripe regions (Howett and Spencer, 2011). From the analysis of VIMS spectra acquired during the same flyby at ~5 km/pixel, temperature variations of crystalline water ice over the Tiger Stripes were at least 20 K [Taffin et al., 2012]: this was done by measuring the strength and center position of the absorption band of crystalline H_2O ice at 1.65 µm (e.g. Grundy and Schmitt, 1998). However, the temperatures between them could not be estimated because water ice is predominantly amorphous in these locations. Measurements from a 74-km altitude flyby by CIRS on April 14, 2012 provided a spatial resolution of 38 m/pixel where the average temperature of 197 K was estimated to come from a 9-m wide fracture (after deconvolution of the point spread function with respect to the size of the fracture) [Goguen et al., 2013]. Locally, temperatures >200K have been measured on Enceladus [Abramov and Spencer, 2009; Goguen et al., 2013].

Temperatures well above 140 K recorded on the active faults may indicate thermodynamic conditions that favor the sublimation of CO_2 ice [McCord et al., 1998]: in fact, free CO_2 ice has a vapor pressure of 1.8 mbar at 140 K and 31 mbar at 160 K [James et al., 1992], whereas for surface temperatures below ~72 K, it may be stable over geological timescales [Watson et al., 1963]. Over time, this difference in surface temperatures between the Tiger Stripes and intermediate terrains may result in the observed pattern in the abundance of CO_2, possibly as the result of migration of free CO_2 ice towards areas with lower surface temperatures [Brown et al., 2006]. Thus the detection of CO_2 ice indicates a transient deposit, and a mechanism of CO_2 replenishment therefore exists at the surface [Brown et al., 2006], similar to Europa [McCord et al., 1998].

4.2 CO_2 compounds on the North Polar Region could come from eruptions on the Tiger Stripes

4.2.1 CO_2 clathrate hydrate deposits may come from blow out eruptions

Formation of CO_2 clathrate hydrates

Fig. 10D and Fig. 11 show relatively deeper absorption band at 4.30 μm in the North Polar Region that could be consistent with CO_2 clathrate hydrates. These hydrates could be formed in in Enceladus' internal ocean [Bouquet et al. 2015], especially structure I (46 H_2O molecules for 1 to 8 CO_2 molecules). The temperature and salinity of the internal ocean likely make CO_2 clathrate sink at the bottom [Safi et al., 2017], and its dissociation may trigger plume eruptions (Kieffer and Xinli, 2006) that are observed over the Tiger Stripes. Given the relatively small amounts of CO_2 measured in the plumes compared to H_2O, the role of CO_2 clathrate hydrates in triggering plume eruptions (which CO_2:H_2O ratio is 0.022 to 0.17) could be a valid assumption.

Venting and deposition mechanisms of CO_2 clathrate hydrates

When a CO_2 gas pocket evacuates ("blows"), fast degassing [Matson et al., 2018] may also entrain some clathrate molecules present in the liquid, which may be vented out by the eruption and be released onto the surface or above the surface. This process requires high velocities at the nozzle, large openings of the ceiling of the gas pocket, and sudden exposure of the surface of the liquid, which is at a temperature near 273 K (Matson et al., 2012), which comes from the constraints on temperature in and out of the plume chambers (Schmidt et al., 2008). However, salt in the ocean in Enceladus with concentrations of NaCl (0.05–0.2 mol.k^{-1}) and the Na-carbonates (0.02–0.1 mol.kg^{-1}) (Postberg et al., 2009) lowers the temperature of the freezing point compared to pure water. Matson et al. (2012) assumes a composition of seawater for Enceladus' internal ocean, which brings the freezing point in Enceladus 2 K lower (271 K) than pure H_2O (273 K). According to (Matson et al., 2012) "in the plume chambers, water vapor is produced which makes up some ninety percent of the gas in the plumes. The heat required to evaporate the water comes from the ocean water passing through the plume chambers. By giving up this heat the ocean water is cooled by 2 K. Since the near-surface ice–seawater interface is at 271 K, this suggests that the ocean water arriving at the plume chambers has a temperature of 273 K." The high venting velocity may allow most of the CO_2 gas to escape. However, a fraction of the population of the much heavier CO_2 clathrate hydrate molecules may not escape from the gravity field of Enceladus, and thus it could be distributed over a large area. CO_2 clathrate hydrates may survive during the eruption and after deposition at temperature near the ocean's surface conditions (~273 K). According to the particle speed probability (Maxwell-Boltzman distribution) the mean speed v_p for a structure I CO_2 clathrate hydrate is $76 < v_p < 88$ m/s (depending on whether one or eight cages contain CO_2 molecules), and for structure II it is $49 < v_p < 52$ m/s. For both cases, these speed estimates are well below the escape velocity of Enceladus (239 m/s). Therefore it might be that blow out eruptions are the source of clathrate venting that might yield deposits. These velocities, however, are high enough for deposition at great distances from the source, even as far as the antipodes.

4.2.2 Stability of CO_2 clathrate hydrates

In low-gravity environment, the escape rate is proportional to the vapor pressure. According to [Smythe, 1975], CO_2 clathrate compounds have vapor pressure several orders of magnitude lower than CO_2 gas alone, which implies that deposits observed today at the surface may correspond to relatively older materials than those consisting of CO_2 ice.

Assuming that CO_2 in the northern hemisphere come from remote sources, the relatively higher concentrations of CO_2 clathrate hydrates in the North Polar Region may indicate that thermodynamical conditions at 60°N latitude and further North favor the stability of that molecular structure. Deposits of CO_2 clathrate hydrates from blow-out eruptions may occur on the entire surface of Enceladus. Over time, the clathrate structures may dissociate faster at lower latitudes than in the polar regions. Consequently, CO_2 clathrate hydrates may accumulate above 60°N. The same phenomenon may occur in the Southern Polar Region, although the average surface temperature may be higher than in the north, due to higher surface thermal flux in the vicinity of active faults. In addition, new deposits of fresh CO_2 ice and H_2O ice may mask any older CO_2 clathrate hydrate deposits.

5. Conclusions

We have related the distribution of CO_2 to the distribution of resurfacing activity of Enceladus by mapping CO_2 surface deposits with near-infrared reflectance spectra from *Cassini* VIMS. The presence of CO_2 ice indicates recent deposition because, at the temperatures measured on Enceladus, CO_2 sublimates rapidly, requiring active replenishment of surface deposits for this constituent to persist over geologically-relevant timescales. Surface CO_2 is therefore compatible with endogenous origin associated with the activity observed in the active faults, from which issue plumes. Our results confirm the highest concentrations of CO_2 are measured in the South Polar Region, where most of the active faults (e.g., the Tiger Stripes) are located, indicating that tectonic activity has some control on the release of CO_2.

The results obtained from our analysis of VIMS spectra support the occurrence of seeping of CO_2 from gas pockets though narrow fissures. The release of pure, cold CO_2 forms ice on the surface near the Tiger Stripes, adjacent to the source vent. Then, local high temperatures (> 130 K on average) favor the sublimation of CO_2, whereas lower temperatures in between and outside the active faults controls the transport and deposition of CO_2 ice. Partial overlay by H_2O ice coming from frequent plume eruption may also enhance the anti-correlation of CO_2-rich materials with respect to the Tiger Stripes and to the H_2O absorption band depths.

In our maps, we can discriminate between CO_2 ice, complexed CO_2 and CO_2 clathrate hydrates, from absorption band depth measurements at four positions between 4.24 and 4.30 μm. The distributions of the four absorption band depths of CO_2 present some obvious similarities at first order, such as the highest concentrations on the South Polar Region, small areas in the North Polar Region, and weaker absorption band depths at mid-latitudes. Those similarities are consistent with the fact that all these absorptions are related to absorbers that share common chemical properties, such as the type of molecule (here it is CO_2).

Some obvious differences exist in the location of maxima and the overall intensity of bands, which is consistent with CO_2-rich materials that differ in chemistry (pure CO_2 ice versus complexed CO_2 or

CO_2 clathrate hydrates). Since complexed CO_2 and CO_2 clathrate hydrates are more stable on the surface of Enceladus than free CO_2 ice, the distribution of the various types of CO_2 deposits is also possibly a function of their relative ages.

Although plume eruptions have been observed by the *Cassini* mission, relatively large amounts of H_2O (96-99%) with respect to CO_2 (0.3-0.8%) have been measured in the plumes (Waite et al., 2017). The strong absorption band depth (up to 40% of the signal in our study) detected on the surface by VIMS suggests a much higher proportion of CO_2 on the surface than in the atmosphere, which is not consistent with the composition of an eruption from a plume chamber. On the other hand, VIMS results are supported by the CO_2 gas pocket model (Matson et al., 2018), because its mechanism of low velocity seep-venting is the only way of delivering pure, cold, CO_2 to the surface where it can form CO_2 ice.. In addition, this model is also compatible with more eruptive blow-out venting of gas pockets that could produce and eject complexed CO_2 away from the South Polar Region. Plume eruptions of H_2O and/or sudden eruption of CO_2 from a gas pocket may drag CO_2 clathrate hydrates (that form in the ocean) and eject them over a very large area around the vent, possibly spreading them over the entire surface of Enceladus. Over time, the lower surface temperatures of the polar regions may favor the accumulation of CO_2 compounds with respect to the mid-latitudes.

Acknowledgments

The helpful suggestions of two anonymous reviewers are gratefully acknowledged. This work has been conducted by the Bear Fight Institute via a contract with the Jet Propulsion Laboratory, California Institute of Technology under a contract with the National Aeronautics and Space Administration. Copyright 2017 Bear Fight Institute. All rights reserved. Government sponsorship acknowledged. Part of this work was performed at the Jet Propulsion Laboratory-California Institute of Technology under contract to NASA.

References

Acton, C.H. (1996) Ancillary Data Services of NASA's Navigation and Ancillary Information Facility; Planetary and Space Science, Vol. 44, No. 1, pp. 65-70.

Blake D.; Allamandola L.; Sandford S.; Hudgins D.; Freund F., 1991, Clathrate hydrate formation in amorphous cometary ice analogs in vacuo, Science 254, 548-551, doi: 10.1126/science.11538372

Bouquet, A.; Mousis, O.; Waite, J. H.; Picaud, S., 2015, Possible evidence for a methane source in Enceladus' ocean, Geophysical Research Letters, 42, 1334-1339, doi: 10.1002/2014GL063013.

R. H. Brown, K. H. Baines, G. Bellucci, J.-P. Bibring, B. J. Buratti, F. Capaccioni, P. Cerroni, R. N. Clark, A. Coradini, D. P. Cruikshank, P. Drossart, V. Formisano, R. Jaumann, Y. Langevin, D. L. Matson, T. B. McCord, V. Mennella, E. Miller, R. M. Nelson, P. D. Nicholson, B. Sicardy and C. Sotin, 2004, The Cassini Visual and Infrared Mapping Spectrometer (VIMS) Investigation, Space Science Reviews 115: 111–168, doi: 10.1007/s11214-004-1453-x.

Brown, R. H.; Clark, R. N.; Buratti, B. J.; Cruikshank, D. P.; Barnes, J. W.; Mastrapa, R. M. E.; Bauer, J.; Newman, S.; Momary, T.; Baines, K. H.; Bellucci, G.; Capaccioni, F.; Cerroni, P.; Combes, M.; Coradini, A.; Drossart, P.; Formisano, V.; Jaumann, R.; Langevin, Y.; Matson, D. L.; McCord, T. B.; Nelson, R. M.; Nicholson, P. D.; Sicardy, B.; Sotin, C., 2006, Composition and Physical Properties of Enceladus' Surface, Science, 311, 1425-1428, doi: 10.1126/science.1121031.

Carlson, R. W., 1999, A tenuous carbon dioxide atmosphere on Jupiter's moon Callisto, Science, 283, 820–821, doi:10.1126/science.283.5403.820.

Chaban, Galina M.; Bernstein, Max; Cruikshank, Dale P., 2007, Carbon dioxide on planetary bodies: Theoretical and experimental studies of molecular complexes, Icarus, 187, 592-599, doi: 10.1016/j.icarus.2006.10.010.

Clark, R., Roush, T., 1984. Reflectance spectroscopy - Quantitative analysis techniques for remote sensing applications. Journal of Geophysical Research 89, 6329–6340.

Clark R. N., Brown R. H., Lytle D. M., 2016, The VIMS Wavelength and Radiometric Calibration, NASA Planetary Data System, Version 1.20.Cruikshank, D. P., Owen T. C., Dalle Ore C., Geballe T. R., Roush T. L., de Bergh C., Sandford S. A., Poulet F., Benedix G. K., Emery J. P., 2005, A spectroscopic study of the surfaces of Saturn's large satellites: H_2O ice, tholins, and minor constituents, Icarus 175, 268-283, doi: 10.1016/j.icarus.2004.09.003.

Clark, R. N.; Swayze, G. A.; Wise, R.; Livo, K. E.; Hoefen, T. M.; Kokaly, R. F.; Sutley, S. J., 2003, A Digital Spectral Library for Planetary and Terrestrial Spectroscopy Analysis, American Astronomical Society, DPS meeting #35, id.19.03; Bulletin of the American Astronomical Society, Vol. 35, p.948

Combe J.-Ph., McCord T. B., Tosi F., Ammannito E., Carrozzo F. G., De Sanctis M. C., Raponi A., Byrne S., Landis M. E., Hughson K. H. G., RAymond C. A., Russell C. T., 2016, Detection of local H_2O exposed at the surface of Ceres, Science 353, doi: 10.1126/science.aaf3010.

Combe J.-Ph., Raponi A., Tosi F., De Sanctis M. C., Carrozzo F. G., Zambon F., Ammannito E., Hughson K. H. G., Nathues A., Hoffmann M., Platz T., Thangjam G., Schorghofer N., Schröder S., Byrne S., Landis M. E., Ruesch O., McCord T., B., Russell C. T., Exposed H_2O-rich areas detected on Ceres with the dawn visible and infrared mapping spectrometer, Icarus, in press, available online since December 17, 2017, doi: 10.1016/j.icarus.2017.12.008.

Cruikshank, Dale P.; Meyer, Allan W.; Brown, Robert H.; Clark, Roger N.; Jaumann, Ralf; Stephan, Katrin; Hibbitts, Charles A.; Sandford, Scott A.; Mastrapa, Rachel M. E.; Filacchione, Gianrico; Dalle Ore, Cristina M.; Nicholson, Philip D.; Buratti, Bonnie J.; McCord, Thomas B.; Nelson, Robert M.; Dalton, J. Brad; Baines, Kevin H.; Matson, Dennis L., 2010, Carbon dioxide on the satellites of Saturn: Results from the Cassini VIMS investigation and revisions to the VIMS wavelength scale, 206, 561-572, doi: 10.1016/j.icarus.2009.07.012.

Dalton, J. B.; Cruikshank, D. P.; Stephan, K.; McCord, T. B.; Coustenis, A.; Carlson, R. W.; Coradini, A., 2010, Chemical Composition of Icy Satellite Surfaces, Space Science Reviews, 153, 113-154, doi: 10.1007/s11214-010-9665-8.

Dougherty, M. K.; Khurana, K. K.; Neubauer, F. M.; Russell, C. T.; Saur, J.; Leisner, J. S.; Burton, M. E., 2006, Identification of a Dynamic Atmosphere at Enceladus with the Cassini Magnetometer, Science, 311, 1406-1409, doi: 10.1126/science.1120985.

Emery, J. P., D. M. Burr, D. P. Cruikshank, R. H. Brown, J. B. Dalton, 2005, Near-infrared (0.8–4.0 µm) spectroscopy of Mimas, Enceladus, Tethys, and Rhea, Astron. Astrophys. 435, 353, doi: 10.1051/0004-6361:20042482.

Filacchione, G.; Capaccioni, F.; Clark, R. N.; Cuzzi, J. N.; Cruikshank, D. P.; Coradini, A.; Cerroni, P.; Nicholson, P. D.; McCord, T. B.; Brown, R. H.; Buratti, B. J.; Tosi, F.; Nelson, R. M.; Jaumann, R.; Stephan, K., 2010, Saturn's icy satellites investigated by Cassini-VIMS. II. Results at the end of nominal mission, Icarus, 206, 507-523, doi: 10.1016/j.icarus.2009.11.006.

Grundy W. M., Buie M. W., Stansberry J. A., Spencer J. R., Schmitt B., 1999, Near-Infrared Spectra of Icy Outer Solar System Surfaces: Remote Determination of H_2O Ice Temperatures, Icarus 142, 536-549, doi: 10.1006/icar.1999.6216.

Grundy W.M. and Schmitt B., 1998. The temperature-dependent near-infrared absorption spectrum of hexagonal H_2O ice. Journal of Geophysical Research: Planets, 103, 25809-25822.

Goguen J. D.; Buratti B. J.; Brown R. H.; Clark R. N.; Nicholson Ph. D.; Hedman M. M.; Howell R. R.; Sotin C.; Cruikshank D. P.; Baines K. H.; Lawrence K. J.; Spencer J.n R.; Blackburn, D. G., 2013, The temperature and width of an active fissure on Enceladus measured with Cassini VIMS during the 14 April 2012 South Pole flyover, Icarus 226, 1128-1137, doi: 10.1016/j.icarus.2013.07.012

Hansen, C. J.; Esposito, L.; Stewart, A. I. F.; Colwell, J.; Hendrix, A.; Pryor, W.; Shemansky, D.; West, R., 2006, Enceladus' Water Vapor Plume, Science, 311, 1422-1425, doi: 10.1126/science.1121254.

Hansen, C. J.; Shemansky, D. E.; Esposito, L. W.; Stewart, A. I. F.; Lewis, B. R.; Colwell, J. E.; Hendrix, A. R.; West, R. A.; Waite, J. H., Jr.; Teolis, B.; Magee, B. A., 2011, The composition and structure of the Enceladus plume, Geophysical Research Letters, 38, doi: 10.1029/2011GL047415.

Hansen, G. B.; Romain, J., 2010, Water Ice Grain Sizes and CO_2 on the Tiger Stripes of Enceladus from Cassini/VIMS Observations, 41st Lunar and Planetary Science Conference, held March 1-5, 2010 in The Woodlands, Texas. LPI Contribution No. 1533, p.2646.

Ingersoll A. P.; Pankine A. A., 2010, Subsurface heat transfer on Enceladus: Conditions under which melting occurs, Icarus, 206, 594-607, doi: 10.1016/j.icarus.2009.09.015.

James P. B., Kieffer H. H., Oaige D. A., 1992, The seasonal cycle of carbon dioxide on Mars, in Mars, edited by H. H. Kieffer, B. M. Jakosky, C. W. Snyder and M. S. Mathews, pp 934-968, Univ. of Ariz. Press, Tucson.

Johnson T. V., 2005, Imaging Enceladus' Exotic South Polar Regions: Imaging Science Team Results, American Geophysical Union, Fall Meeting 2005, abstract id.P21F-03.

Kieffer, S. W.; Xinli L.; et al., 2006, A Clathrate Reservoir Hypothesis for Enceladus' South Polar Plume, Science. 314, 1764–1766, doi:10.1126/science.1133519.

Mastrapa, R. M.; Bernstein, M. P.; Sandford, S. A., 2005, Near Infrared Spectra of Mixtures Relevant to Icy Satellite, American Geophysical Union, Fall Meeting 2005, abstract #P11B-0109

Matson, D. L.; Castillo-Rogez, J. C.; Davies, A. G.; Johnson, T. V., 2012, Enceladus: A hypothesis for bringing both heat and chemicals to the surface, Icarus, 221, 53-62 doi: 10.1016/j.icarus.2012.05.031.

Matson, D. L.; Davies, A. G.; Johnson, T. V.; Combe, J.-Ph.; McCord, T. B.; Radebaugh, J.; Singh, S., 2018, Enceladus' near-surface CO2 gas pockets and surface frost deposits, Icarus 302, 18-26, doi: 10.1016/j.icarus.2017.10.025.

McCord, T. B.; Carlson, R.; Smythe, W.; Hansen, G.; Clark, R.; Hibbitts, C.; Fanale, F.; Granahan, J.; Segura, M.; Matson, D.; Johnson, T.; Martin, P., 1997, Organics and other molecules in the surfaces of Callisto and Ganymede, Science, 278, 271-275, doi: 10.1126/science.278.5336.271.

McCord, T. B.; Hansen, G. B.; Clark, R. N.; Martin, P. D.; Hibbitts, C. A.; Fanale, F. P.; Granahan, J. C.; Segura, M.; Matson, D. L.; Johnson, T. V.; Carlson, R. W.; Smythe, W. D.; Danielson, G. E., 1998, Non-water-ice constituents in the surface material of the icy Galilean satellites from the Galileo near-infrared mapping spectrometer investigation, Journal of Geophysical Research, 103, 8603-8626, doi: 10.1029/98JE00788.

Mennella, V.; Palumbo, M. E.; Baratta, G. A., 2004, Formation of CO and CO2 Molecules by Ion Irradiation of Water Ice-covered Hydrogenated Carbon Grains, The Astrophysical Journal, 615, 1073-1080, doi: 10.1086/424685.

Oancea, A.; Grasset, O.; Le Menn, E.; Bollengier, O.; Bezacier, L.; Le Mouélic, S.; Tobie, G., 2012, Laboratory infrared reflection spectrum of carbon dioxide clathrate hydrates for astrophysical remote sensing applications, Icarus 221, 900-910, doi: 10.1016/j.icarus.2012.09.020.

Porco, C. C.; Helfenstein, P.; Thomas, P. C.; Ingersoll, A. P.; Wisdom, J.; West, R.; Neukum, G.; Denk, T.; Wagner, R.; Roatsch, T.; Kieffer, S.; Turtle, E.; McEwen, A.; Johnson, T. V.; Rathbun, J.; Veverka, J.; Wilson, D.; Perry, J.; Spitale, J.; Brahic, A.; Burns, J. A.; Del Genio, A. D.; Dones, L.; Murray, C. D.; Squyres, S., 2006, Cassini Observes the Active South Pole of Enceladus, Science, 311, 1393-1401, doi: 10.1126/science.1123013.

Safi, E.; Thompson, S. P.; Evans, A.; Day, S. J.; Murray, C. A.; Parker, J. E.; Baker, A. R.; Oliveira, J. M.; van Loon, J. Th., 2017, Properties of CO2 clathrate hydrates formed in the presence of MgSO4 solutions with implications for icy moons, Astronomy & Astrophysics, 600, doi: 10.1051/0004-6361/201629791.

Sandford, S. A.; Allamandola, L. J., 1990, The physical and infrared spectral properties of CO2 in astrophysical ice analogs, Astrophysical Journal, 355, 357-372, doi: 10.1086/168770.

Schmidt, J., Brilliantov, N., Spahn, F., Kempf, S., 2008. Slow dust in Enceladus' plume from condensation and wall collisions in tiger stripe fractures. Nature 451, 685– 688.

Scipioni, F.; Schenk, P.; Tosi, F.; D'Aversa, E.; Clark, R.; Combe, J.-Ph.; Ore, C. M. Dalle, 2017, Deciphering sub-micron ice particles on Enceladus surface

Smythe W. D., 1975, Spectra of hydrate frosts: their application to the outer solar system, Icarus 24, 421-427, doi: 10.1016/0019-1035(75)90059-7.

Stegman D. R.; Freeman J.; May D. A., 2009, Origin of ice diapirism, true polar wander, subsurface ocean, and tiger stripes of Enceladus driven by compositional convection, Icarus, 202, 669-680, doi: 10.1016/j.icarus.2009.03.017.

Taffin, C.; Grasset, O.; Le Menn, E.; Bollengier, O.; Giraud, M.; Le Mouélic, S., 2012, Temperature and grain size dependence of near-IR spectral signature of crystalline water ice: From lab experiments to Enceladus' south pole, Planetary and Space Science, 61, 124-134, doi: 10.1016/j.pss.2011.08.015.

Waite, J. Hunter; Combi, Michael R.; Ip, Wing-Huen; Cravens, Thomas E.; McNutt, Ralph L.; Kasprzak, Wayne; Yelle, Roger; Luhmann, Janet; Niemann, Hasso; Gell, David; Magee, Brian; Fletcher, Greg; Lunine, Jonathan; Tseng, Wei-Ling, 2006, Cassini Ion and Neutral Mass Spectrometer: Enceladus Plume Composition and Structure, Science, 311, 1419-1422, doi: 10.1126/science.1121290.

Waite, J. H., Jr.; Lewis, W. S.; Magee, B. A.; Lunine, J. I.; McKinnon, W. B.; Glein, C. R.; Mousis, O.; Young, D. T.; Brockwell, T.; Westlake, J.; Nguyen, M.-J.; Teolis, B. D.; Niemann, H. B.; McNutt,

R. L.; Perry, M.; Ip, W.-H., 2009, Liquid water on Enceladus from observations of ammonia and ^{40}Ar in the plume, Nature, 460, 487-490, doi: 10.1038/nature08153.Waite, J. Hunter; Glein, Christopher R.; Perryman, Rebecca S.; Teolis, Ben D.; Magee, Brian A.; Miller, Greg; Grimes, Jacob; Perry, Mark E.; Miller, Kelly E.; Bouquet, Alexis; Lunine, Jonathan I.; Brockwell, Tim; Bolton, Scott J., 2017, Cassini finds molecular hydrogen in the Enceladus plume: Evidence for hydrothermal processes, Science 356, 155-159, doi: 10.1126/science.aai8703.

Watson K.; Murray B. C.; Brown H., 1963, The stability of volatiles in the solar system, Icarus 1, 317-327, doi: 10.1016/0019-1035(62)90030-1.

Appendix

Like most datasets collected by spacecraft instruments, VIMS data have imperfections that require more careful treatment as time passes and the analyses become more sensitive. In this study, data calibration has been under particular scrutiny, because precise positioning of each observed pixel is critical, and because the signal-to-noise in the range 4.24–4.28 µm is generally low. We have investigated several calibration issues and developed techniques for improving them in this case. These techniques could be generalized to be used by other studies and perhaps on the entire VIMS data set.

Of particular concern is how the VIMS infrared wavelengths have shifted over time (Fig. A1), as revealed by monitoring narrow lines of known position in Titan's and Saturn's atmospheres (Clark et al., 2016) (http://wwwvims.lpl.arizona.edu/Howitworks.html). We compensate for this variation by a two-step process. 1) A value for this wavelength shift is calculated at the time of the acquisition of any VIMS spectrum, assuming a linear interpolation between each point measured in Fig. A1. 2) VIMS spectra are resampled in the spectral dimension from the shifted wavelength to the original wavelengths.

Table 1: Summary of VIMS observations processed to create global maps of Enceladus.

Orbit number	First file number	Last file number	Number of observations
7	1484523993	1484533914	6
8	1487255888	1487302144	29
9	1489028159	1489087241	34
11	1495319119	1495363657	10
12	1500040056	1500069702	85
16	1511777815	1511784548	25
17	1514140705	1516171358	70
21	1530343833	1530346698	10
23	1536531398	1536534584	10
25	1541727375	1541728777	15
31	1561728480	1561728480	1
43	1597166869	1597180353	37
44	1600379685	1602294224	95
45	1604152328	1604184588	128
46	1606886709	1606891734	10
52	1627326410	1627330202	3
54	1634223108	1635855445	47
55	1637449785	1637482463	96
60	1652848938	1652874475	73
61	1656976036	1656976650	2
62	1660420386	1660446670	52
65	1669819228	1671608635	74
66	1675144005	1675152950	27
70	1694646956	1699270828	303
71	1702359426	1702362997	17
72	1710055594	1711575441	34

73	1713110172	1713115977	155
90	1816669056	1820438640	52
91	1823501373	1824733761	53
92	1829231340	1831438809	165
93	1834200478	1834214488	42

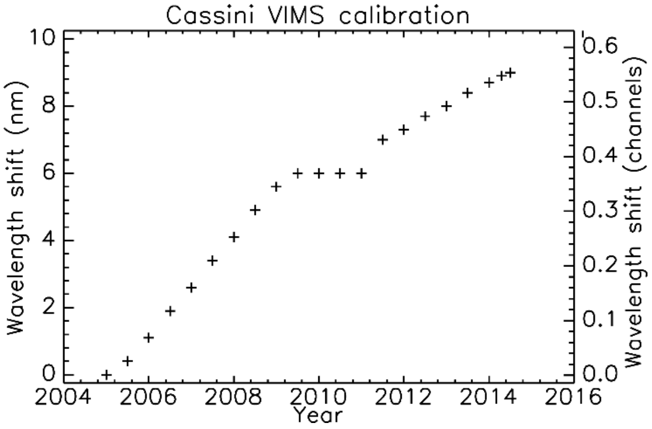

Fig. A1: VIMS wavelength shift as a function of time.

5.1 A.1 VIMS calibration

5.1.1 A.1.1 Dark current correction

In VIMS data, a measurement of the electronic dark current is acquired at the beginning of the sequence corresponding to one line of the final image cube. Reading and processing VIMS data can be done in a standard way using routines of the Integrated Software for Imagers and Spectrometers (ISIS, https://isis.astrogeology.usgs.gov/). The dark current correction for the VIMS infrared detector consists of reading the sideplane data and subtracting this from the input cube. In ISIS, the default correction from the VIMSCAL procedure is a simple subtraction from the raw DNs of the dark current values. Optionally, it is possible to apply the dark current with a linear fit instead of the default subtraction.

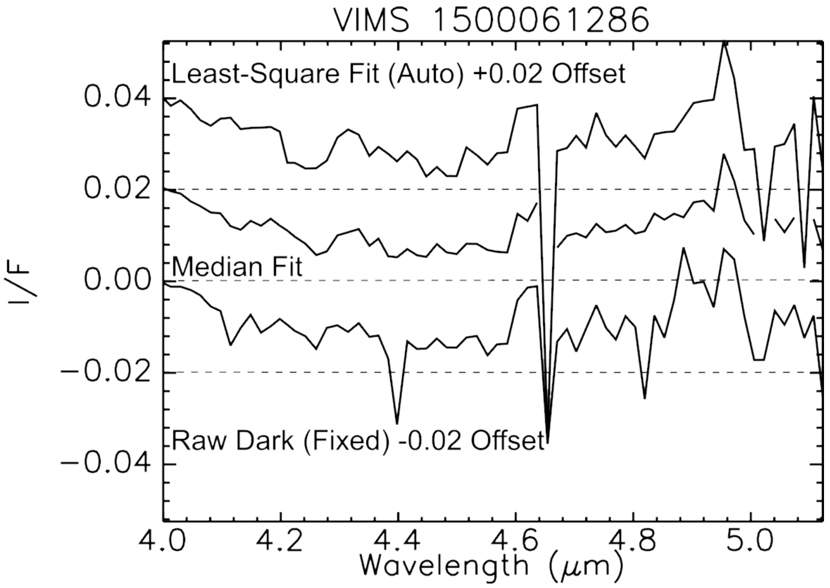

Fig. A2: : One example of a VIMS spectrum calibrated with three dark current corrections. In the VIMSCAL procedure of ISIS, the Raw Dark and Linear Fit Dark options may result in negative values (erroneous). The median is the one we use in this study.

We tested the two options and we have identified various occurrences of negative values in the data as a result (Fig. A2). Negative values in I/F are invalid, which proves errors in the calibration process. Analysis of these errors helped us understand the cause and develop a workaround (Fig. A3).

The VIMS dark current is affected by occasional spurious data that deviate from the expected trend between the first and last line of a given file (Fig. A3). These deviations are excessive compared to the measured DNs over the surface target. The simple subtraction of the measured dark current results in spikes in the spectra (Fig. A2) and horizontal striping of VIMS images (Fig. A4A). On the other hand, the optional linear fit of the VIMSCAL procedure is sensitive to outlying points caused by spikes in the data (Fig. A3), which may also results in excessive correction of the dark current. This overcorrection creates excessive absorption band depth (Fig. A4B) and sometimes negative I/F values between 4.24 and4.28 μm.

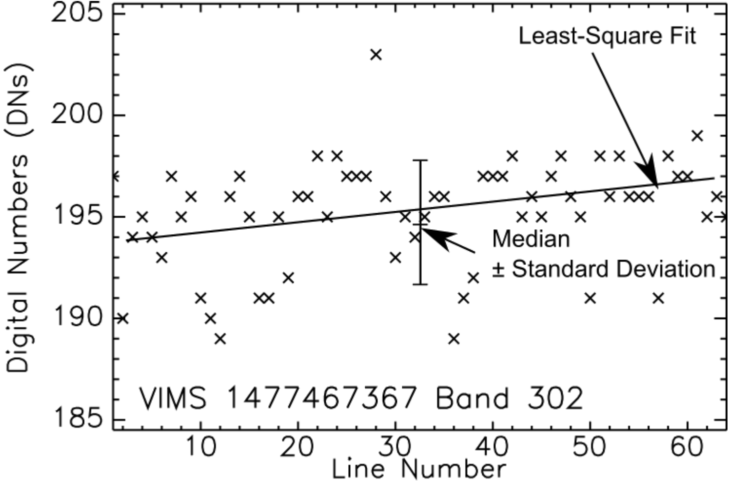

Fig. A3: VIMS Dark Current (DNs) as a function of line number and corrections. Calibration options publicly available either in the PDS or in ISIS include a subtraction of the measured dark current (default), or a least-square linear fit of the measured dark current as a function of the line

number. Both methods are affected by outlying points in the data, which create artifacts in the calibrated data. An improved correction proposed in this study relies on the median value of the dark current as a function of the line number.

Fig. 12:

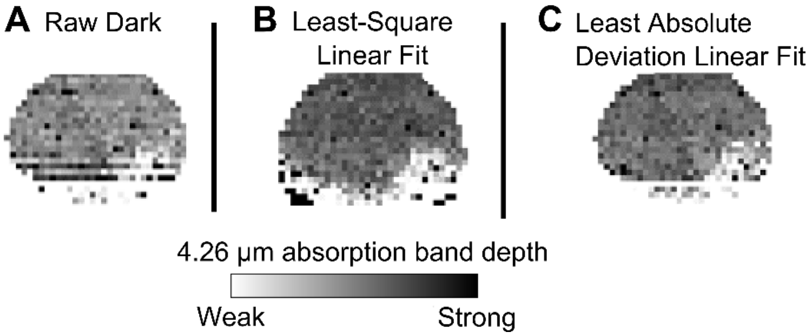

Fig. A4: VIMS images showing the effects of three different dark current corrections. A – Subtraction of the Raw Dark. B – Least-squares linear fit. C – Least absolute deviation linear fit (this study).

We have developed a dark current correction that relies on the median value of the measured points, which is less sensitive to outlying points due to spikes in the data (Fig. A3). As a result, negative I/F values are mostly eliminated (Fig. A2), and images have better spatial coherence (Fig. A4C).

5.1.2 A.1.2 Calculation of geographic coordinates

Although ISIS provides tools for mapping VIMS data, such as the PHOCUBE routine, the outcome is limited to one set of coordinates (pixel center latitude and longitude) for each pixel. However, each VIMS pixel can be large compared to the size of Enceladus, and the area covered by each pixel can vary a great deal in size and shape (Fig. A5). Thus, the location of the center of each pixel is not accurate enough to map the CO_2 distribution over linear features such as the Tiger Stripes.

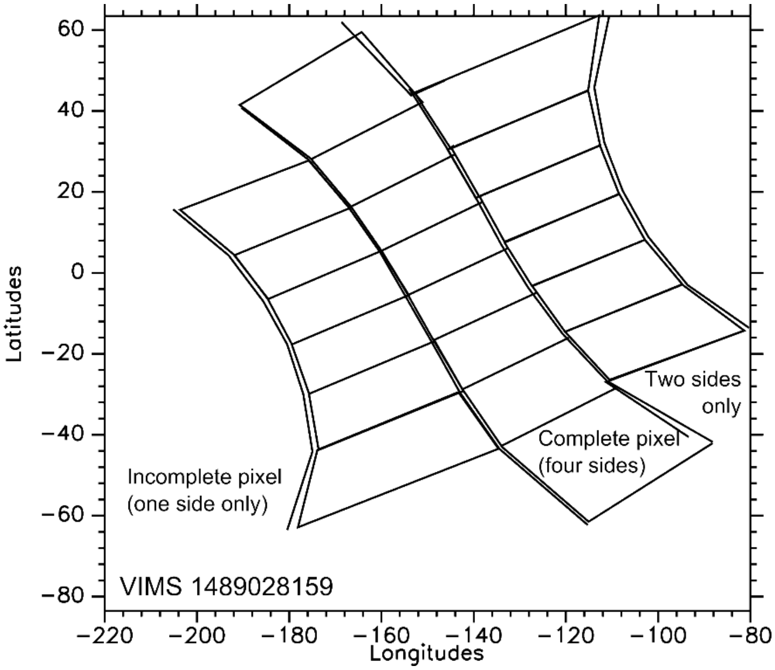

Fig. A5: Schematic view of the projection of VIMS pixels of one VIMS observation on Enceladus. It shows the geographic coordinates for each pixel is necessary for mapping accurately the surface of Enceladus.

In order to improve the mapping of VIMS data, we calculated the coordinates of each corner of each pixel using data and routines from the Navigation and Ancillary Information Facility (NAIF) SPICE system (Acton, 1996). We used a package that is compatible with IDL (Interactive Data Language, by Harris Geospatial), which is available as a toolkit (https://naif.jpl.nasa.gov/naif/toolkit_IDL.html). The data needed to calculate the coordinates are the spacecraft ephemeris, planet ephemerides, instrument description and pointing which are also made publicly available by NAIF and have the generic name of SPICE kernels (http://naif.jpl.nasa.gov/pub/naif/CASSINI/kernels/). Based on the design of VIMS (Fig. A6) described in Brown et al. (2004) and in (http://www.ifsi-roma.inaf.it/cassini/downloads/VIMS-paper.pdf), we have developed an IDL program that calls the routines of the NAIF toolkit, reads the SPICE kernels and calculates the geographic coordinates for each corner of each pixel, both at the start and stop times of the acquisition. In addition, the program calculates the incidence, emergence and phase angles and the geographic coordinates for the center of each pixel. Based on these geometric parameters, we have been able to validate our calculations against results provided by the PHOCUBE routine of ISIS.

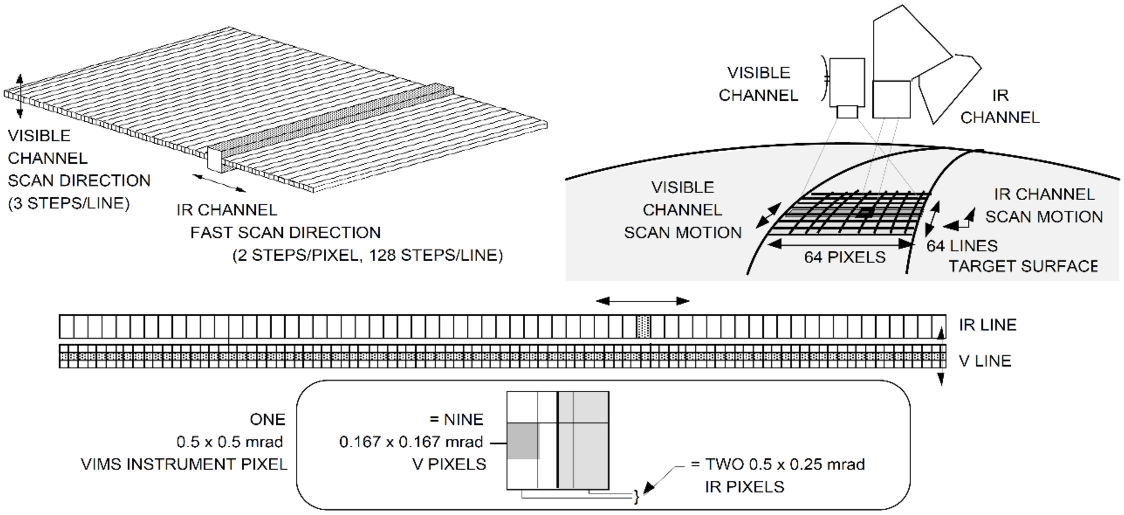

Fig. A6: VIMS pixel synthesis and image scanning (http://www.ifsi-roma.inaf.it/cassini/downloads/VIMS-paper.pdf).